Article

Photo-Induced Super-Hydrophilicity of Nano-Calcite @ Polyester Fabric: Enhanced Solar Photocatalytic Activity against Imidacloprid

Ambreen Ashar,○ Ayesha Qayyum,○ Ijaz Ahmad Bhatti, Humera Aziz,* Zeeshan Ahmad Bhutta,* Mostafa A. Abdel-Maksoud, Muhammad Hamzah Saleem, and Mohamed R. Eletmany
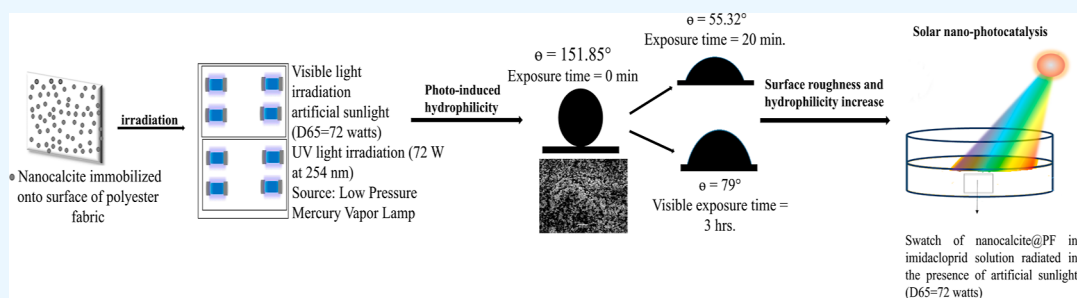
Read Online

ACCESS | 📊 Metrics & More | 📰 Article Recommendations

ABSTRACT: The present study is pertinent to photo-induced, hydrophilic, nano-calcite grown onto the mercerized surface of polyester fabric (PF), treated with UV (10−50 min) and visible light (1−5 h) in addition to its photocatalytic application. The wicking method has been employed to select the most hydrophilic sample of fabric upon irradiation. The micrographs obtained by scanning electron microscopy, transmission electron microscopy, and high-resolution transmission electron microscopy indicated the erosions occurring at the surface of nano-calcite after UV light irradiation, maintaining the crystallinity of the photocatalyst. The surface charge has been measured for as-fabricated and irradiated nano-calcite @ PF for the development of high negative zeta potential after UV light irradiation (−24.6 mV). The irradiated nano-calcite @ PF exhibited a significant change in its contact angle, and the wetting property was enhanced to a considerable extent on UV (55.32°) and visible light irradiation (79.00°) in comparison to as-fabricated nano-calcite @ PF (137.54°). The irradiated samples of nano-calcite @ PF delineated the redshift in harvesting of solar spectrum, as revealed by diffuse reflectance spectroscopy comparative spectra. Additionally, the band gap of untreated nano-calcite was found to be 3.5 eV, while UV- and visible light-irradiated PF showed a reduction in band gap up to 2.95 and 3.15 eV upon UV and visible light irradiation. The photocatalytic efficiency of mesoporous nano-calcite was evaluated by photocatalytic degradation of imidacloprid as the probe pollutant. Higher solar photocatalytic degradation of imidacloprid (94.15%) was attained by UV light-irradiated nano-calcite @ PF. The time-resolved photoluminescence study has verified the high photocatalytic activity of UV light-irradiated nano-calcite @ PF for the generation of high concentration of hydroxyl radicals. The highly efficient reusability of a nano-calcite-based solar photocatalytic reactor has been observed for 10 cycles of treatment of imidacloprid bearing wastewater. The enhanced photocatalytic activity of UV light-exposed (20 min), superhydrophilic, nano-calcite @ PF for mineralization of pollutants suggests it to be an efficient solar photocatalyst for environmental applications.

1. INTRODUCTION

The contaminated environment caused by organic pollutants along with population growth and industrialization is becoming an overwhelming problem around the world. Owing to the magnificent dilapidation of ecosystem caused by increased demographic extension, efforts of scientists are required for the advantage of our earth. A neo-nicotinoid natural insecticide synthetically obtained from nicotine present in tobacco was familiarized during 1990s to substitute organo-phosphorous and carbamate insecticides.[1] It has been declared to be relatively less toxic to vertebrates and humans with a range of employments such as plant safety, pest resistance, animal well-being, and protection of aquatic ecosystem.

Imidacloprid insecticide is considered as an agonist of nicotinic acetylcholine receptors present in the nervous system. Upon exposure to imidacloprid, it binds to the receptors, causing depolarizing blockade leading to paralysis and death of insects. The nicotine-based receptors are located merely within the central nervous system, in the case of insects. However, they

are present at the neuro-muscular junctions and the central nervous system in vertebrates[2] Although imidacloprid is selectively toxic to insects, it is considered to bear moderate to high toxicity to birds and mammals as its exposure results in tremors, muscular weaknesses, and ataxia.[2,3]

The high solubility of imidacloprid in water renders it a potential contaminant of the water reservoirs.[4] The minimization of its potential hazards and harmful effects requires treatment of imidacloprid-containing wastewaters using an appropriate method. An extensive research has been executed to remove imidacloprid from effluents including physical, chemical, and biological methods.[4,5]

The most promising technique for the degradation of organic pollutants that are deteriorating water quality is photocatalysis.[6,7] At present, in context to the research regarding nano-scaled materials, researchers are seeking special interest on nanostructures as they are potentially organized, extremely sensitive, and effective due to quantum confinement. They possess a higher surface to volume ratio and a smaller grain size as compared to those of bulk materials. In the level of nanoscale, the electrical and optical properties change due to band gap variation, rendering materials suitable for new devices and applications.[8] The photocatalyst can be irradiated to produce hydroxyl radicals, which are capable of attacking the recalcitrant organic molecules to degrade them into innocuous products. The core benefits of photocatalysis include ease in procedure, low budget for conduction and maintenance, and ecofriendly nature[9] The photocatalytic degradation of imidacloprid is carried out on the surface of nano photocatalysts by ensnaring OH• radicals into the active sites.[10]

Visible light-driven heterogeneous photocatalysis exhibit many perks like (1) use of sustainable free-of-cost light resource, i.e., sunlight, (2) high rate of photocatalytic oxidation reaction with low consumption of energy, and (3) natural ambiance with mild reaction conditions as compared to those in other traditional technologies of water treatment.[11] The realized application of photocatalysis faces the the operational issue related to the use of powdered photocatalysts in a slurry reactor, which is a main bottleneck. Precisely, when the photocatalytic nanoparticles are stirred into the slurry, they are to be removed after the completion of reaction. The wastewater treatment requiring the recovery of the photocatalyst from the treated solution is not only time-consuming but also costly and dreary, causing reduction in the advantages of performance.[12]

To evade the post-performance regaining of the photocatalyst for the treatment of upcoming batches of effluents, the nanoparticles can be immobilized onto a suitable stationary support. The fabrics made from flax,[13] cotton,[14] nylon,[15] wool,[16] and polyester[17] being potential candidates have been reported as an appropriate photocatalyst support owing to stability, flexibility, high surface area, and cost effectiveness. Among all types of fabrics, the polyester fabric is the most feasible one because of its tensile strength, resistance to UV light and chemicals, optimum stretch ability, and low shrinking and wrinkling tendency.[18]

By using functionalization and surface treatment, researchers are generally trying to achieve good dispersibility by the induction of polar groups like −OH, −COOH, and (−C-(O)−), which contribute toward polar solvents.[19] Hydrophilicity is a surface phenomenon that depends on the oxygen vacancies in the crystal lattice usually created by generating defect sites of oxygen.[20] The enhancement of surface hydrophilicity causes the acceleration of photocatalytic surface degradation of the organic pollutants adsorbed onto the surface of nanophotocatalysts, i.e., metal oxides. Since the phenomenon of hydrophilicity is pertinent to the interface between the liquid and solid surfaces, the surface variation can significantly affect the adsorption of pollutants. In short, the efficiency of the photocatalytic reaction occurring on the surface of the photocatalyst depends upon its surface properties.[21]

After the UV−visible light irradiation, the gaseous oxygen present on the surface accelerates the photodegradation of the adsorbed molecules based on the enhancement of surface hydrophilic behavior.[22] The transfer of photoenergy to the molecules causes an increase in a range of new moieties such as ions, photons, metastable free radicals, and ultraviolet radiations.[23] Under the UV light irradiation, the hydrophilic conversion is due to an increase in the degradation of contiguous water molecules and adsorption of −OH onto the surface of the photocatalyst adhered to the substrate.

Ultraviolet light irradiation of a nano-scaled metal oxide produces a highly hydrophilic surface due to the structural changes of the metal oxide itself and the substrate.[24] Development of a photo-created energy gap, which is established for the processing of photocatalytic reaction, directs water and oxygen in the ambience to produce a high yield of reactive oxygen species possessing a strong oxidation potential. Hence, the improvement in the photocatalytic efficiency of the hydrophilic surface depends on the gaseous oxygen chemisorbed onto the photocatalyst's surface. The accelerated photocatalytic degradation of the adsorbed pollutants on the surface can be attributed to a large number of closely spaced hydrophilic domains arising upon UV light illumination.

After irradiating the photocatalyst with ultraviolet light, the water contact angle with the surface decreases, and water instigates to spread all over its surface.[22,25] The surface energy, which affects the interaction between the solid and liquid interface, depends upon the creation and spread of droplets on a thin film and can be determined by the contact angle measurement.[26] The surface can be made highly wettable through changes in the external parameters such as temperature and surface morphological properties. All applications of fabricated thin films and other nanostructures depend on the controlled and desired surface morphology.[27]

The solid surface wettability is based on the roughness of the surface and the chemical configuration.[28] The features related to surface properties of the photocatalyst include crystalline phase, surface defects, number of surface-bound hydroxyl groups, and surface acidity. However, a pronounced influence of the OH− groups on the chemical properties of a photocatalyst is based on the surface roughness and defects. The reports have stated that erosion of the photocatalyst surface can upsurge the adsorption of the polar molecules and ultimately increase the rate of the photocatalytic reaction.[29,30]

In the present work, nano-calcite has been grown onto the mercerized surface of polyester fabric (PF); the modification of surface hydrophilicity has been investigated via UV−visible light irradiation that strongly modified its surface properties. The photo-induced hydrophilicity of the nano-calcite photocatalyst grafted onto the surface of PF has been determined by irradiating it for different time intervals to examine the impact of light on the surface hydrophilicity. Furthermore, the UV light-irradiated nano-calcite @ PF exhibited a better photo-

catalytic performance toward the solar photocatalytic degradation of the insecticide (imidacloprid) as compared to that of as-fabricated nano-calcite @ PF.

2. RESULTS AND DISCUSSION

2.1. Characterization of Nano-Calcite @ PF. The UV light- and visible light-irradiated samples are first subjected to wicking test to determine the increase in the hydrophilicity of the samples. Among all the irradiated samples, the ones exhibiting the highest wickability owing to enhanced hydrophilicity were selected for further characterization techniques.

2.2. Wickability Analysis of Nano-Calcite @ PF. The wicking analysis is executed by a spontaneous transposition of the liquid in the solid interface having a capillary system. The wicking rate of the fabric depends on the pore size, pore distribution, and hydrophilic groups present onto the surface.[32] To enhance the hydrophilicity of nano-calcite @ PF, UV−visible light irradiation pretreatments were applied. During such treatments, the number of hydroxyl groups onto the irradiated surface of fabric was enhanced due to the breakage of the hydroxyl bonds of adhered water, which in turn improved fiber hydrophilicity.[33] Wickability results of the surface-grown nano-calcite @ PF irradiated with UV−visible light are shown in Figure 1a,b. The swatches of surface-grown
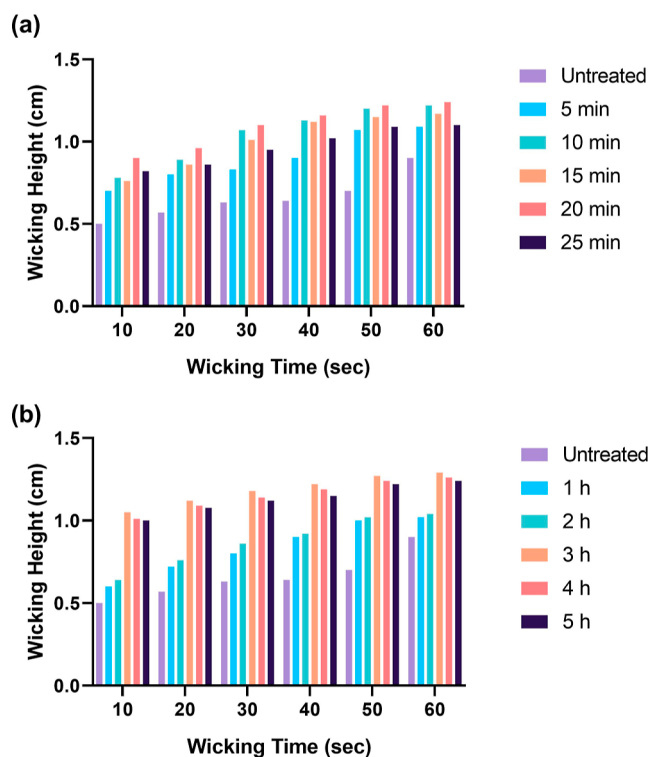

Figure 1. Wickability of (a) UV light-irradiated nano-calcite @ PF and (b) visible light-irradiated nano-calcite @ PF in water.

nano-calcite @ PF (5×5 cm^2) treated with ultraviolet light irradiation (20 min) and visible light irradiation nano-calcite @ PF (3 h) exhibited a highest wicking rate among all the irradiated samples.

2.3. Crystalline Nature, Crystallite Size, and Phase Analysis. The crystalline nature, crystallite size, and phase purity of the as-fabricated and irradiated nano-calcite @ PF were examined via X-ray diffractometry (XRD) as displayed in

Figure 2. The various crystallographic planes of the subjected nanomaterial can be observed at 18.67 (001), 23.1 (012), 29.3
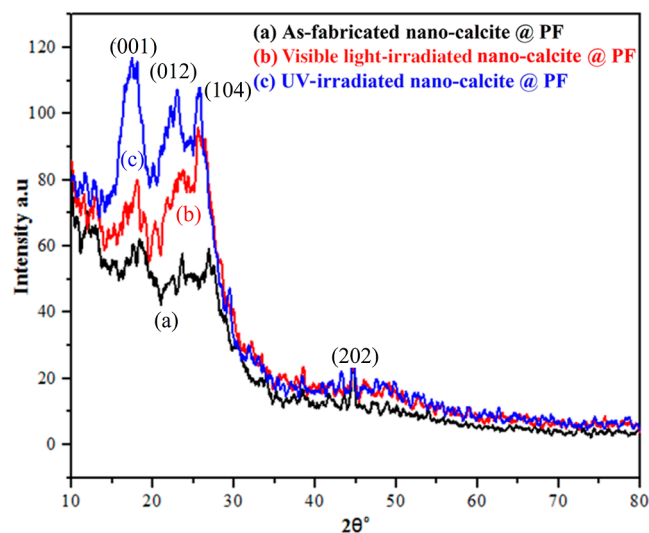

Figure 2. XRD of (a) as-fabricated nano-calcite @ PF, (b) visible light-irradiated nano-calcite @ PF, and (c) UV light-irradiated nano-calcite @ PF.

(104), 33.96 (101), 43.1 (202), 47.1 (018), and 47.5° (116). All the above-mentioned planes strongly support the nano-calcite phase according to X-pert HighScore software, exhibiting close agreement with the standard file (JCPDS-05-0586) for nano-calcite. In addition to the peaks of nano-calcite, the peaks for nano-lime Ca(OH)$_2$ and CaO also appeared, which rendered the material multiphasic. However, the peak at 29.3° (104) represents the crystal face, which belongs to calcite Ca (CO$_3$)$_2$,[31] so the dominating phase according to MATCH software was nano-calcite. After irradiating, the intensity of the peak increased, which exhibited improved crystallinity. The average crystallite size of the synthesized and irradiated sample of nano-calcite @ PF was measured using the highest peak of nano-calcite @ PF at (104). Using Debye−Scherer's formula (eq 1), the average crystallite size of the as-fabricated, visible light- (3 h), and UV light (20 min)-irradiated samples of nano-calcite @ PF was found to decrease as 38.45, 31.36, and 23. 67 nm, respectively.

$$L = \frac{k\lambda}{\beta \cos \theta}$$

(1)

2.4. Structural Analysis of Nano-Calcite @ PF. The chemical composition of as-fabricated and irradiated nano-calcite @ PF was confirmed using Fourier transform infrared spectrum, which is given in Figure 3a−c. In the given spectrum, a narrow peak at 3449 cm^{-1} appeared due to the stretching vibration of the O−H group. The bands at 873, 1080, and 1464 cm^{-1} appeared because of the different −CO vibrational modes of the CO$_3^{2-}$ group. Furthermore, a small peak at 2352 cm^{-1} appeared due to the absorbed gaseous CO$_2$, as indicated by prior research report.[34] The bands at 710, 872, 1081, 1420, and 1795 cm^{-1} displayed the common characteristic features of CaCO$_3$, which indicated the asymmetric vibration of the C−O bond.[35] Figure 3c shows the spectrum of UV light-irradiated nano-calcite @ PF having a sharp peak intensity at 3449.54 cm^{-1} indicating the high surface density of the −OH groups. The increment in the adsorption intensity
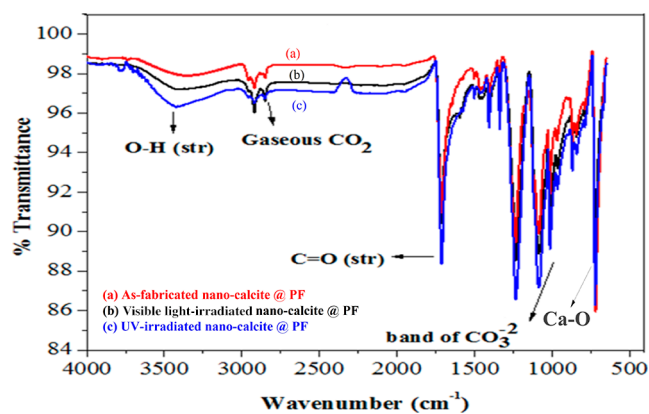
Figure 3. FTIR spectrum of (a) as-fabricated nano-calcite @ PF, (b) visible light-irradiated nano-calcite @ PF, and (c) UV light-irradiated nano-calcite @ PF.

reveals the presence of more acidic groups. Further, a minor reduction at 1490 cm^{-1} in the adsorption intensity was observed in Figure 3c relative to Figure 3a,**b** due to bending vibrations of the C−H bond in the methylene group. Herein, the proportion of oxygen-comprising groups like −COOH, C=O, and C−OH increased on the irradiated surface of nano-calcite @ PF. The fabric surface of nano-calcite @ PF was modified from hydrophobic to hydrophilic as the oxygen-comprising groups increased on the surface, which is in accordance with already reported results.[36] These facts may be attributed to some defected C−C bands present at the modified surface of nano-calcite @ PF broken by irradiation treatment. Hence, it is observed from the comparison of the peak area of the −OH group that the density of the hydroxyl group on the surface of nano-calcite @ PF was highly increased by ultraviolet irradiation treatment. The peak at 750 cm^{-1} delineated the Ca−O bending for all samples; i.e., the irradiated and as-fabricated samples had almost the same peak position and peak area, indicating that irradiation did not affect the Ca−O bond.

2.5. Morphological Characteristics of Nano-Calcite @ PF. The morphological modification in the nano-calcite @ PF structure caused after irradiation treatment was studied by comparison of as-fabricated and irradiated nano-calcite @ PF as presented in Figure 4 (a−d). It can be shown in micrograph that the surface of as-fabricated nano-calcite as functionalized polyester was entirely and densely covered with monomodal particles of nano-calcite (Figure 4a). The micrograph of nano-calcite covering the as-fabricated functionalized polyester fabric is provided in Figure 4b, showing the spherical shape of nano-calcite having a smooth surface with nominal roughness.[37] On UV−visible light irradiation of nano-calcite @ PF, the roughness of the surface increased due to the erosions of boundaries of discoid particles. However, upon visible light irradiation, some erosions occurred on the surface of nano-calcite, indicated by the presence of fluffy agglomerated nanostructures (Figure 4c). However, after UV light irradiation, the surface erosions increased magnificently creating ridges onto the surface of nano-calcite (Figure 4d). Moreover, the morphology of nano-calcite also transformed from discoid to rod- or string-like nanostructures. It has been reported that surface roughness magnified the concentration of the −OH groups, which appeared as the presence of small grooves and kinks on the surface of nano-calcite @ PF (Figure 4c,d).[38] The internal structure and shape of nano-calcite have
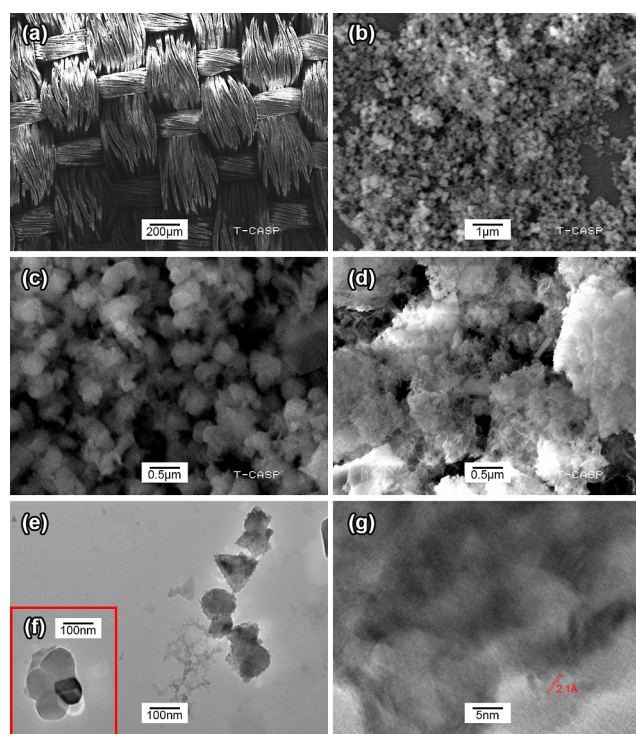

Figure 4. Micrographs of (a) functionalized polyester with grafted nano-calcite, (b) nano-calcite densely covering the surface of polyester fabric, (c) visible light-irradiated nano-calcite @ PF, and (d) UV light-irradiated nano-calcite @ PF; (e) TEM of UV light-irradiated nano-calcite; (f) TEM of as-fabricated nano-calcite; and (g) HRTEM of UV light-irradiated nano-calcite.

been determined by transmission electron microscopy (TEM) of as-fabricated and UV light-treated nano-calcite (Figure 4e,f). The TEM micrographs indicate that before UV light irradiation, the surface of the spherical nanostructures was smooth, but after UV irradiation, the groves and kinks developed on the surface of treated nano-calcite. Furthermore, the smaller discoids joined together to adopt the shape of nano strings or rods. Regarding the internal crystalline structure of UV-treated nano-calcite, high-resolution TEM (HRTEM) indicated the monocrystalline structure with a line spacing of 2.1 Å (Figure 4g). The high crystallinity of nano-calcite revealed by HRTEM supported the diffractogram of nano-calcite @ PF. The results were similar with those from previously reported research.[37]

2.6. Surface Properties of Nano-Calcite @ PF. Nano-particles have a charged surface that attracts a thin layer of ions of opposite charge toward its surface. The charge density of a surface depends on OH$^-$ and H$^+$ concentrations. Prior research proposed that the zeta potential (ZP) of the calcite material is created due to the presence of the Ca^{2+}, CO_3^{2-}, HCO_3^-, H$^+$, and OH$^-$ ions on the surface.[39] Zeta potentials are obtained from electrophoretic mobility according to the Smoluchowski equation (eq 2).

$$\zeta = \frac{\eta\mu}{\varepsilon} \tag{2}$$

where ζ is the zeta potential, η is the viscosity of solution, μ is the electrophoretic mobility, and ε represents the dielectric constant.[40] After the irradiation treatment, the value of zeta potential was enhanced, and charge on the surface produced upon UV light irradiation was higher than that produced by
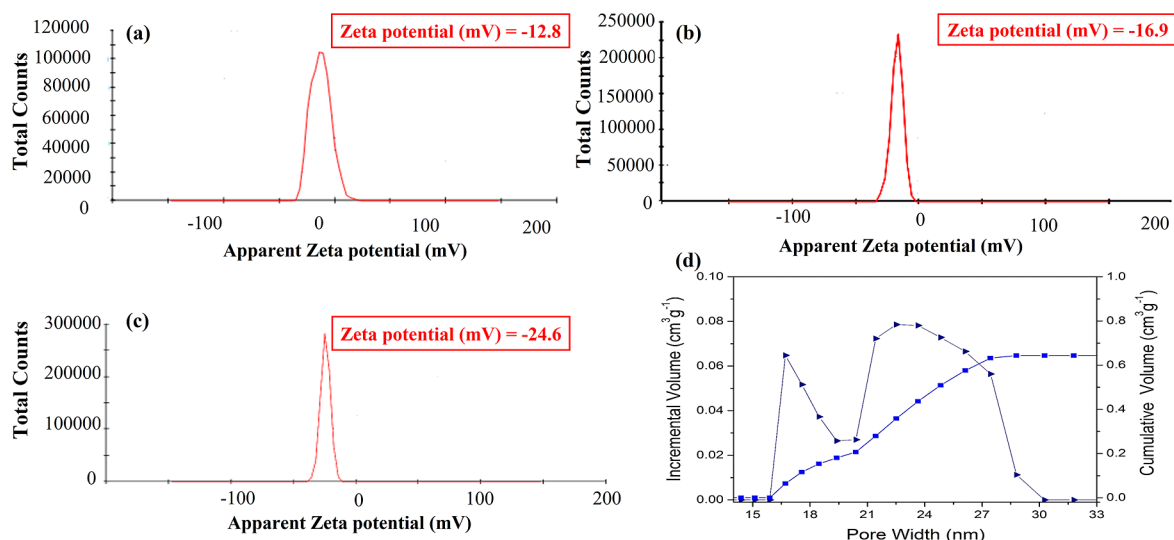
Figure 5. Zeta potential of (a) as-fabricated nano-calcite, (b) visible light-irradiated nano-calcite, and (c) UV light-irradiated nano-calcite and (d) pore size distribution curve of UV light-irradiated nano-calcite.
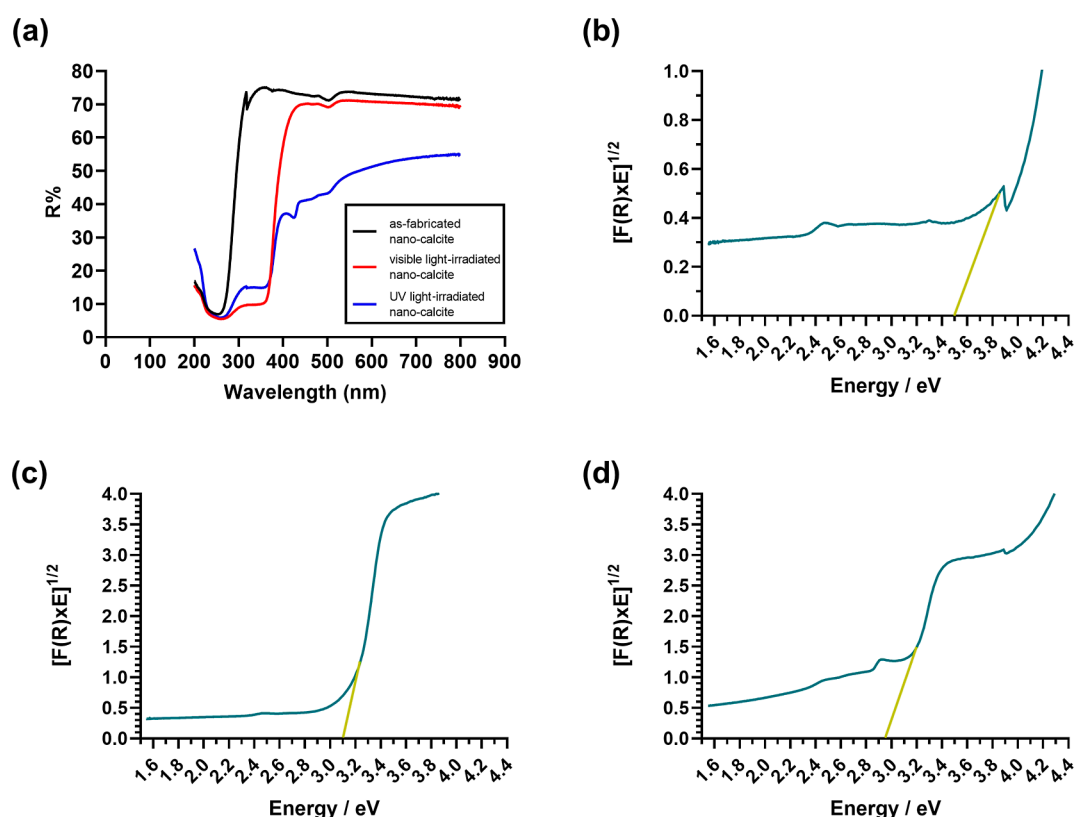

Figure 6. (a) Comparative diffused reflectance spectra of as-fabricated and UV light-irradiated nano-calcite @ PF and band gap of (b) as-fabricated nano-calcite @ PF, (c) visible light-irradiated nano-calcite @ PF, and (d) UV light-irradiated nano-calcite @ PF.

visible light irradiation of surface-grown nano-calcite @ PF. Nano-calcite @ PF shows zeta potential variation from −12.8 to −24.6 mV in Figure 5a−c as the value for as-fabricated nano-calcite @ PF was −12.8, −16.9 mV for visible light-irradiated (irradiation time = 3 h) and −24.6 mV for UV light-irradiated (irradiation time = 20 min) samples, when measured in their aqueous suspension. The surface of nano-calcite @ PF turned anionic, when nano-calcite came in contact with water, and an increase in surface charge occurred that led to the absorption of the high-density−OH groups onto the surface of nano-calcite @ PF. Conclusively, the zeta potential of as-fabricated, UV−visible light-irradiated nano-calcite @ PF turned negative, attracting imidacloprid toward it for chemisorption. Moreover, the zeta potential of surface-grown nano-calcite @ PF was observed to be associated with the surface electrical conductivity of semiconductor materials.[41] The measured photoconductivity of as-fabricated, visible light-irradiated, and UV-light irradiated nano-calcite was 0.081, 0.326, and 0.724 mS/cm, respectively. It can be concluded that the increased number of photogenerated charge carriers moved
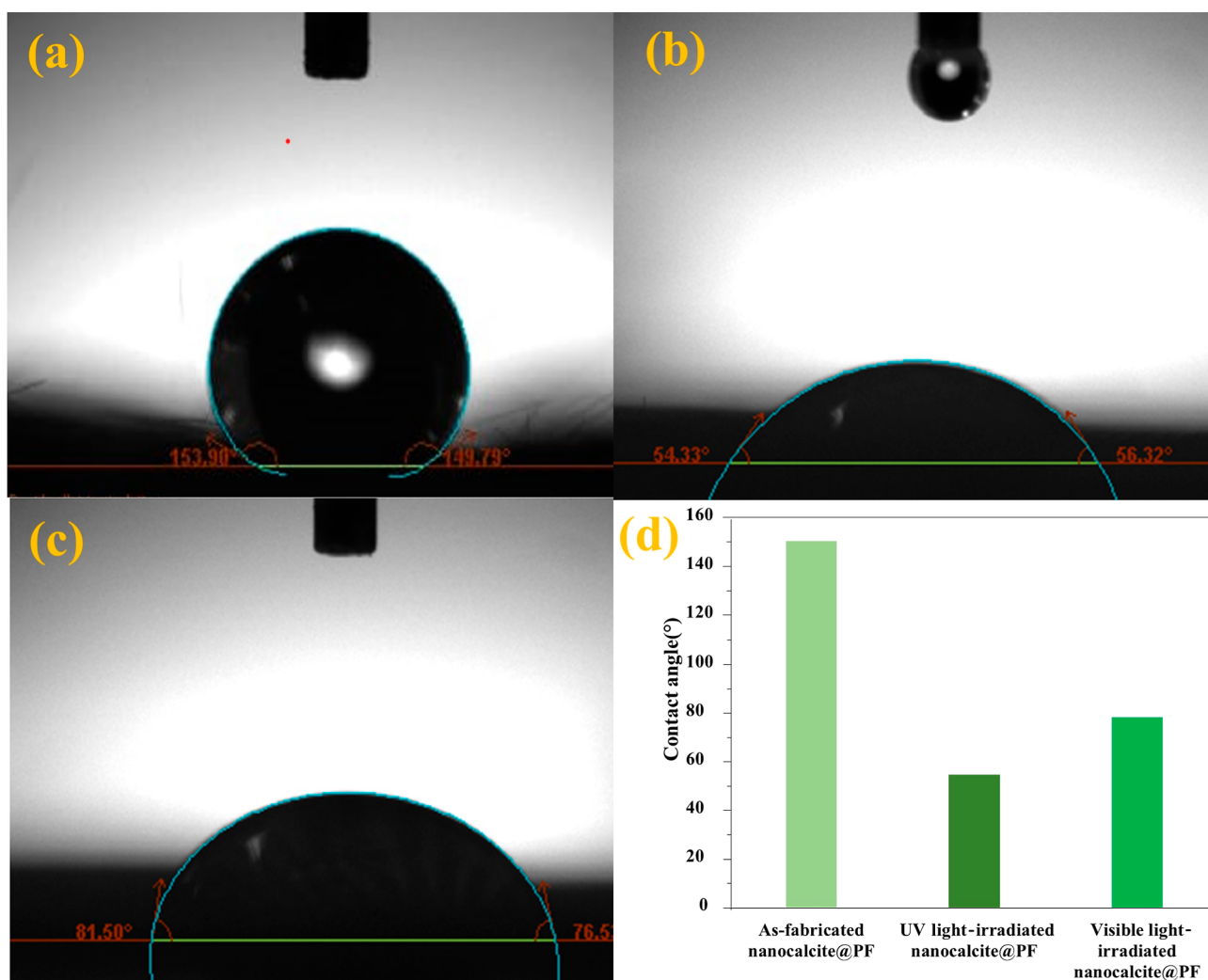
Figure 7. Average water contact angle of (a) as-fabricated nano-calcite @ PF, (b) UV light-irradiated nano-calcite @ PF, and (c) visible light-irradiated nano-calcite @ PF and (d) comparison of the contact angle value of as-fabricated and irradiated nano-calcite @ PF.

to the surface of the photocatalyst causing the enhancement in the photoconductivity of nano-calcite @ PF after UV light irradiation.[42]

The pore width and pore volume of the nano-calcite sample have been determined using the Barret−Joyner−Halenda (BJH) pore size distribution plot. The pore size varied from 16 to 32 nm for the sample, which can be clearly assessed from the graph (Figure 5d). The maximum pore volume for the sample was 0.65 cm^3/g. The results have declared that nano-calcite was mainly mesoporous, and it was found suitable for the chemisorption of imidacloprid molecules. According to previous research, mesoporous nano structures are beneficial for the diffusion of reactants and products in the reaction mixture.[43]

2.7. Optical Properties of Nano-Calcite @ PF. The diffuse reflectance spectroscopic study of nano-calcite @ PF delineated that 70% of solar light was reflected above 280 nm, and the band gap edge shifted from 280 to 390 nm after the irradiation treatment (Figure 6a). Moreover, the % reflectance spectrum of UV light-irradiated nano-calcite exhibited the capability of the fabricated nano-calcite @ PF sample to harvest more than 50% of the visible portion of solar radiation.[38] The high visible light harvesting tendency can be attributed to increased surface erosions upon UV light

irradiation and enhanced hydrophilic domains on the surface based on the induction of the−OH groups.[44]

The greater tendency of the UV light-irradiated sample to harvest solar radiations in comparison to those of visible light-irradiated and as-fabricated nano-calcite @ PF was further confirmed by band gap energy.[45] The band gap energy of as-fabricated nano-calcite @ PF was 3.5 eV as shown in Figure 6b, calculated by the Kubelka−Munk plot using the given relation (eq 3); Figure 6c shows the band gap for visible light-irradiated nano-calcite @ PF to be 3.1 eV, while Figure 6d displays further reduction in the band gap for UV light-irradiated nano-calcite @ PF (2.95 eV), which exhibited an absorption edge at 390 nm falling in the visible range of solar spectrum.

$$[(R_\infty)E]^{1/2} = A(h\nu - E_g) \tag{3}$$

where R_∞ is the diffuse reflectance.[46] The reduction in the band gap can be explained based on surface roughness, oxygen vacancy, and inter-band energy states, which were created below the conduction band.[47,48] Consequently, the electron requires less energy to get excited to the conduction band (CB) from the valence band (VB).[49] The photodegradation of imidacloprid in the presence of the solar photocatalyst, nano-

calcite @ PF, can be assigned to the high generation rate of electron−hole pairs.

2.8. Evaluation of the Extent of Hydrophilicity of Nano-Calcite @ PF. The as-fabricated and irradiated surfaces of nano-calcite @ PF were investigated with contact angle measurement for determination of the extent of hydrophilicity. The contact angle is used to determine the surface energy and surface tension of solids along with their wettabilities. The contact angle of water drop on the nano-calcite @ PF surface was measured using optical tensiometers by a sessile drop method. The surface is considered more hydrophilic, if the angle is less than 90° and the water droplet can spread more onto the surface.[50] The water contact angles of the as-fabricated, UV−visible light-irradiated nano-calcite @ PF swatches are given in Figures 7a−c, 6d, and Table 1 explains the comparison of reduction in the contact angle.

Table 1. Variation in Water Contact Angle of the As-Fabricated and UV−Visible Light-Irradiated Nano-Calcite @ PF

functionalized polyester fabric	angles between the water droplet and nano-calcite @ PF surface		average of the angles between the water droplet and nano-calcite @ PF surface
			$\dfrac{\theta_1 + \theta_2}{2}$
	θ_1 (deg)	θ_2 (deg)	(deg)
As-fabricated	153.90	149.79	151.85
UV light-irradiated	54.33	56.32	55.32
Visible light-irradiated	81.50	76.5	79

2.9. Solar Photocatalytic Degradation of Imidacloprid and Optimization of Reaction Parameters. Based on the development of strong photo-induced hydrophilicity, the efficiency of the UV light-irradiated nano-calcite @ PF (20 min) photocatalyst was investigated by the solar photocatalytic degradation of imidacloprid as a suitable probe. Response surface methodology was used to optimize the variable reaction parameters for the solar photocatalytic degradation of imidacloprid. A response of 20 runs were obtained by UV/vis absorption spectrometry and were put in the 2nd-order polynomial equation (eq 4)[29,51] as displayed in Table 2.

$$Y = 67.57 - 125A + 2.87B + 3.80C - 0.22AB - 3.93AC$$
$$- 0.83BC - 9.28A^2 - 6.62B^2 - 6.01C^2 \qquad (4)$$

where Y is the % age degradation of imidacloprid and A, B, and C are used to indicate the exposure time of sunlight, pH, and H_2O_2 concentrations, respectively.

Figure 8 displays the interaction between the reaction parameters mentioned above. Figure 8a shows 64% degradation at pH = 11 and a sunlight exposure time of 3h, while H_2O_2 concentration remained constant. Figure 8b presents 63.50% degradation at pH = 11 and 30 mM H_2O_2 concentration. Figure 8c shows a plot of 3D surface between irradiation time and concentration of H_2O_2, according to which upon 3h of irradiation using 30 mM of H_2O_2, the maximum degradation achieved was 65.25%. The optimized parameters had a vital role in the degradation of the insecticide; the extent of degradation showed a significant rate of solar photocatalytic reaction under these optimized conditions. It is clear that the

Table 2. Central Composite Design with Reaction Variable Values and Percent Degradation of Imidacloprid

run	A	B	C	% degradation
1	1.00	11.00	50.00	55.1
2	1.00	7.00	50.00	55.34
3	3.00	9.00	3.64	48.12
4	3.00	9.00	30.00	75.5
5	1.00	11.00	10.00	45
6	3.00	9.00	30.00	63.24
7	3.00	9.00	30.00	64
8	1.00	7.00	10.00	39
9	3.00	5.64	30.00	40
10	3.00	9.00	30.00	70.9
11	0.36	9.00	30.00	47.4
12	5.00	11.00	50.00	42.7
13	5.00	7.00	50.00	40.7
14	6.36	9.00	30.00	42.5
15	3.00	12.36	30.00	57.5
16	5.00	7.00	10.00	43
17	5.00	11.00	10.00	45.23
18	3.00	9.00	65.64	59.2
19	3.00	9.00	30.00	72.56
20	3.00	9.00	30.00	63

degradation rate is accelerated on adding up to 30 mM of H_2O_2 because of the increase in the generation of OH• radicals. The extent of solar photocatalytic degradation of imidacloprid was enhanced on elevating the concentration of H_2O_2 causing in situ generation of a large amount of OH• radicals.[52] Contrarily, further increase in oxidant concentration, beyond the optimum level, resulted in retardation of the solar photocatalytic degradation rate of a probe pollutant, even on extending the irradiation time.[47] The solar irradiation time is also a prime factor having an important role in the photocatalytic degradation rate of imidacloprid. With the increase in radiation time, the magnitude of the photocatalytic degradation was increased due to harvesting more photons, generating a substantially large number of e/⁻h+ pairs. Herein, the rate of photodegradation increased upon increasing the exposure of reaction contents from 1 to 3 h, but upon extending exposure time further, no significant enhancement in photocatalytic degradation occurred. The limitation observed can be attributed to the magnitude of solar energy harvested and increased recombination of the electron−hole pairs. Up to pH 11, the extent of the photocatalytic degradation enhanced, while further increase in pH lowered the degradation rate. It can be concluded that the solar photocatalytic degradation rate of imidacloprid accelerated at alkaline pH in comparison to neutral and acidic pH.

Analysis of variance (ANOVA) table shows the significant effect of the reaction parameters with value of probability $F = 0.0013$, predicted $R^2 = 0.8840$ with adjusted $R^2 = 0.776$, and C.V = 9.33%, showing that the model applied was significant. The values provided by Design Expert software are shown in Table 3.

The comparison of the rate of solar photocatalytic degradation of imidacloprid using as-fabricated and UV light-irradiated nano-calcite @ PF, under optimized conditions (pH = 11, sunlight irradiation time = 3 h, and concentration of oxidant = 30 mM) was investigated. In the graph of C_t/C_0, treated solution of imidacloprid (30 ppm, 100 mL) ($\lambda_{max} = 269.5$ nm) by non-functionalized PF, as-fabricated nano-calcite
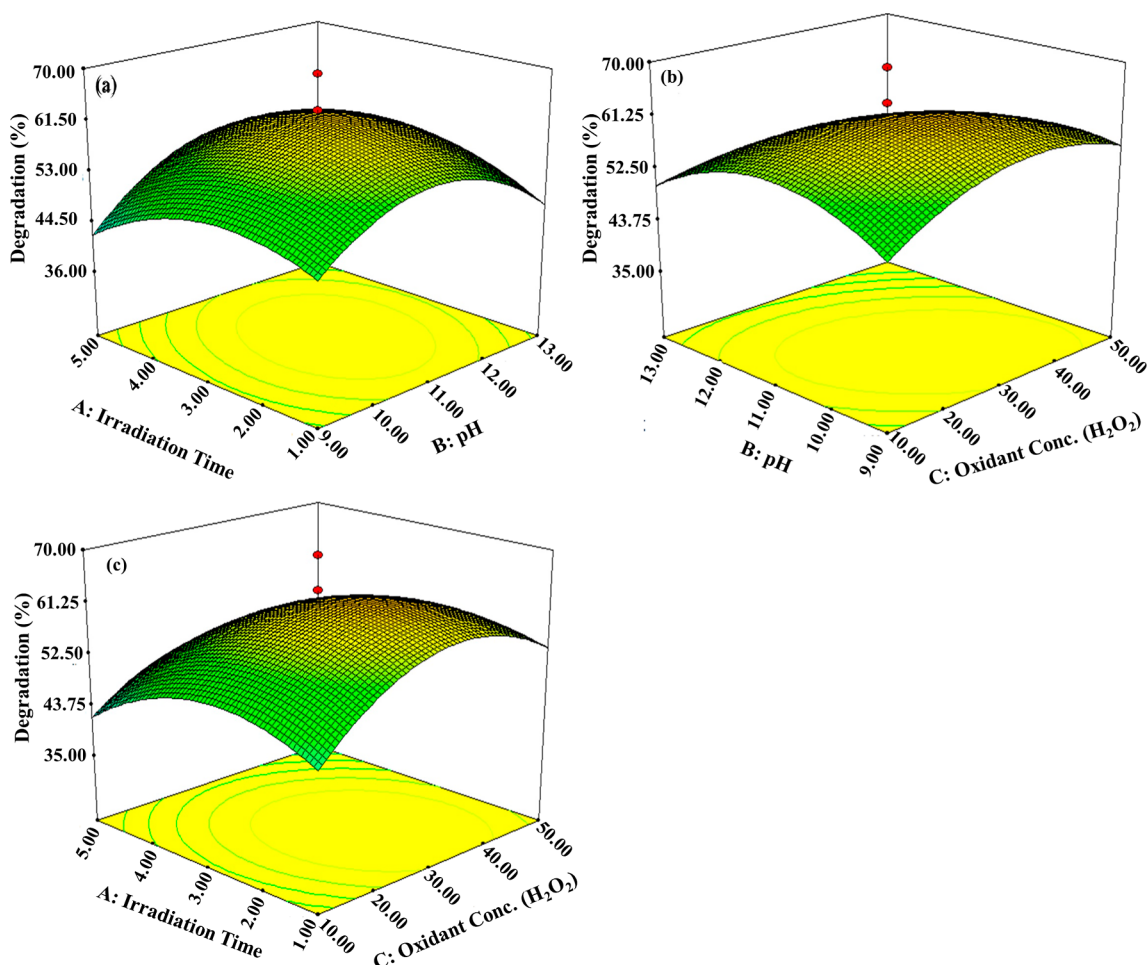
Figure 8. 3D response surface plots of interactive effects (a) irradiation time and pH, (b) pH and concentration of the oxidant, (c) irradiation time and concentration of the oxidant, showing the interactive effect of the independent variable of %degradation of imidacloprid treated with UV light-irradiated nano-calcite @ PF.

Table 3. ANOVA for Central Composite design (CCD) Showing % Age Degradation of Imidacloprid Treated with UV Light-Irradiated Nano-Calcite @ PF

source	sum of squares	d.f	mean square	F value	P-value prob > F	
model	2311.83	9	256.87	8.47	0.0013	significant
irradiation Time	18.87	1	18.87	0.62	0.4486	
pH	112.64	1	112.64	3.71	0.0829	
oxidant conc	175.12	1	175.12	5.77	0.0372	
AB	0.37	1	0.37	0.012	0.9138	
AC	123.80	1	123.80	4.08	0.0710	
BC	5.56	1	5.56	0.18	0.6776	
A^2	921.86	1	921.86	30.38	0.0003	
B^2	639.78	1	639.78	21.09	0.0010	
C^2	386.87	1	386.87	12.75	0.0051	
residual	303.41	10	30.34			
lack of fit	154.54	5	30.91	1.04	0.4842	not significant
pure error	148.87	5	29.77			
core total	2615.23	19				
std dev. = 4.51		C.V = 9.33%		R^2 = 0.8840		adj R^2 = 0.776

@ PF, oxidant-bearing non-functionalized PF, and UV light-irradiated nano-calcite @ PF has been compared. It is obvious from the graph that there was no decrease in C_t/C_0 with respect to time for imidacloprid solution on immersing non-functionalized PF, and almost the same trend was shown on the addition of H_2O_2 to the swatch of non-functionalized PF

(as the control). The decrease in the C_t/C_0 value for imidacloprid was obtained using as-fabricated nano-calcite @ PF reaching 0.42 mg/L in 210 min of sunlight irradiation. The enhancement in the photocatalytic degradation of imidacloprid after adding the photocatalyst demonstrated that the h[+] and OH[•] radicals were the main active species.[53,54] However, the

photocatalytic degradation of imidacloprid on using as-fabricated nano-calcite @ PF was lesser as compared to that on using UV light irradiated (exposure time = 20 min) nano-calcite @ PF, which was 0.12 mg/L; the data obtained by kinetics conveyed that the maximum % degradation of the probe pollutant obtained was 85.50 and 94.15% for as-fabricated and irradiated nano-calcite @ PF, respectively, in 210 min as shown in Figure 9.
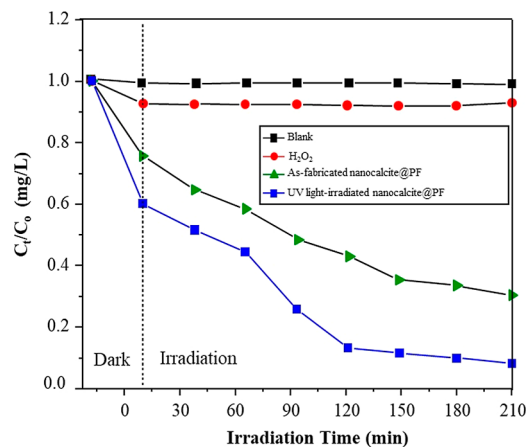

Figure 9. Determination of the extent of photocatalytic degradation (C_t/C_0) of imidacloprid, (concentration of H_2O_2 30 mM, pH 11) with respect to time, upon irradiation under artificial sunlight, using as-fabricated and UV light-irradiated nano-calcite @ PF.

2.10. Evaluation of the Extent of Solar Photocatalytic Degradation of Imidacloprid.
As-fabricated and UV light-irradiated nano-calcite @ PF were compared to check the degradation rate of the imidacloprid solution immersed in the insecticide solution (imidacloprid, 30 ppm). Since the swatch of nano-calcite @ PF exhibited the maximum rate of imidacloprid degradation after UV light irradiation, evaluation of the degradation rate of imidacloprid-bearing wastewater sample was done using UV−visible spectroscopy, high-performance liquid chromatography (HPLC), and FTIR using UV light-irradiated nano-calcite @ PF. The absorbance of the insecticide (30 ppm solution of imidacloprid)-containing wastewater sample was measured by a UV−visible spectrophotometer as shown in Figure 10a. After the exposure to artificial sunlight for 210 min, the absorbance of the untreated and treated imidacloprid solutions with UV light-irritated nano-calcite @ PF was 1.882 and 0.11, respectively. The decomposed product of the insecticide solution was monitored by the decrease in the absorption peak at 269.5 nm.

According to Figure 10b, in the FTIR spectra of the untreated and treated imidacloprid solutions (30 ppm), the control peaks were observed at 3128.49, 1240.27, and 1566.25 cm^{-1} for the O−H stretching vibration band of C═N and vibration band of N═N.[53,55] Figure 10c shows the HPLC chromatogram of the untreated and treated imidacloprid solutions (30 ppm, 20 μL). The reduction in peak height, peak area, and shift in peak position of insecticide (imidacloprid) in the effluent was examined as indicated in previous reports.[56] Due to $\pi-\pi^*$ of the nitro guanidine chromophore, the imidacloprid wavelength (270 nm) was found to be the most appropriate for the detection of imidacloprid solution in the context of peak area or peak height.[57] The retention time and peak area of treated imidacloprid decreased due to its

degradation into a smaller nontoxic hydrocarbon.[58] Table 4 shows retention time, peak area, and peak height of the treated and untreated imidacloprid solutions.

2.11. Determination of the OH• Radical Generated by Nano-Calcite @ PF.
The concentration of the OH• radical generated by UV light-irradiated nano-calcite @ PF has been determined through time--resolved photoluminescence study of aqueous solution of 2, hydroxy terephthalic acid exposed to D65 = 72 watt for 100 min. On excitation of irradiated hydroxy terephthalic acid at 316 nm, the emission peak appeared at 426 nm. The extent of the rise of the emission peak indicated the increase in concentration of hydroxy terephthalic acid and OH• radicals generated in 100 min. It was observed that the rate of generation of OH• radicals increased with respect to the time of exposure of nano-calcite @ PF to artificial sunlight (Figure 10d). The higher hydrophilicity and presence of the increased number of −OH groups attached to the surface (polar facets (001) and (101)) of nano-calcite consequently caused the generation of excess of OH•. The previous reports have shown similar results.[59]

2.12. Reusability of Nano-Calcite @ PF.
The photo-stability and durability of functionalized polyester-based solar photocatalytic reactor have been determined by repeating the solar photocatalytic reactions. 10 batches of imidacloprid-containing wastewater were treated with nano-calite @ PF under optimized reaction conditions. The values of C/C^0 were measured, and the graph is added to explain the efficiency of the irradiated solar photocatalytic reactor in 10 cycles (Figure 11). It is quite obvious from the bar graph that even after 8 cycles, the reduction in the % degradation was reduced up to 91.34%.

2.13. Mechanism of Photocatalytic Degradation of Imidacloprid.
Figure 12 displays the schematic illustration for the degradation of imidacloprid by UV light-irradiated nano-calcite @ PF. The decrease in the band gap energy upon UV light irradiation caused remarkable generation of electron−hole pairs as charge carriers, resulting in an enhanced rate of degradation of imidacloprid, as indicated by the UV/visible spectrum of untreated and treated imidacloprid. When the surface of UV light-irradiated nano-calcite @ PF is exposed to sunlight, the electrons of the VB get excited to produce photogenerated e$^-$/h$^+$ pairs. However, the excited e$^-$ from CB and h$^+$ from VB can be recombined, and in that case, light energy is dissipated in the form of heat, as shown in eq 5. When a suitable trapping agent, i.e., H_2O and O_2, is present at/near the surface of the photocatalyst, a redox reaction occurs. The photogenerated e$^-$ reacts with the surface-adsorbed oxygen and water molecules, which are not only involved in redox reaction but also the additional source of the •OH radical on the surface of the photocatalyst, as shown in eqs 6 and 7.[60]

Figure 13 shows the degradation of an imidacloprid molecule (1) to compound nitroso-compound and further shows the formation of intermediate molecules (2, 3, and 4). The cleavage of the C−N bonds of compound (4) degrade into imidazolidine-2-imine and 3-methylpyridine, which ultimately degrade into smaller compounds carbon dioxide, ethylene diamine, acrolein, and ammonia. According to the proposed reaction mechanism, UV light-irradiated nano-calcite @ PF catalyst absorbs UV−visible light radiation from the natural sunlight to excite the electron from VB to CB to generate electrons and holes. The generated electrons reacted with oxygen dissolved in water form superoxide anions (•O_2^-),

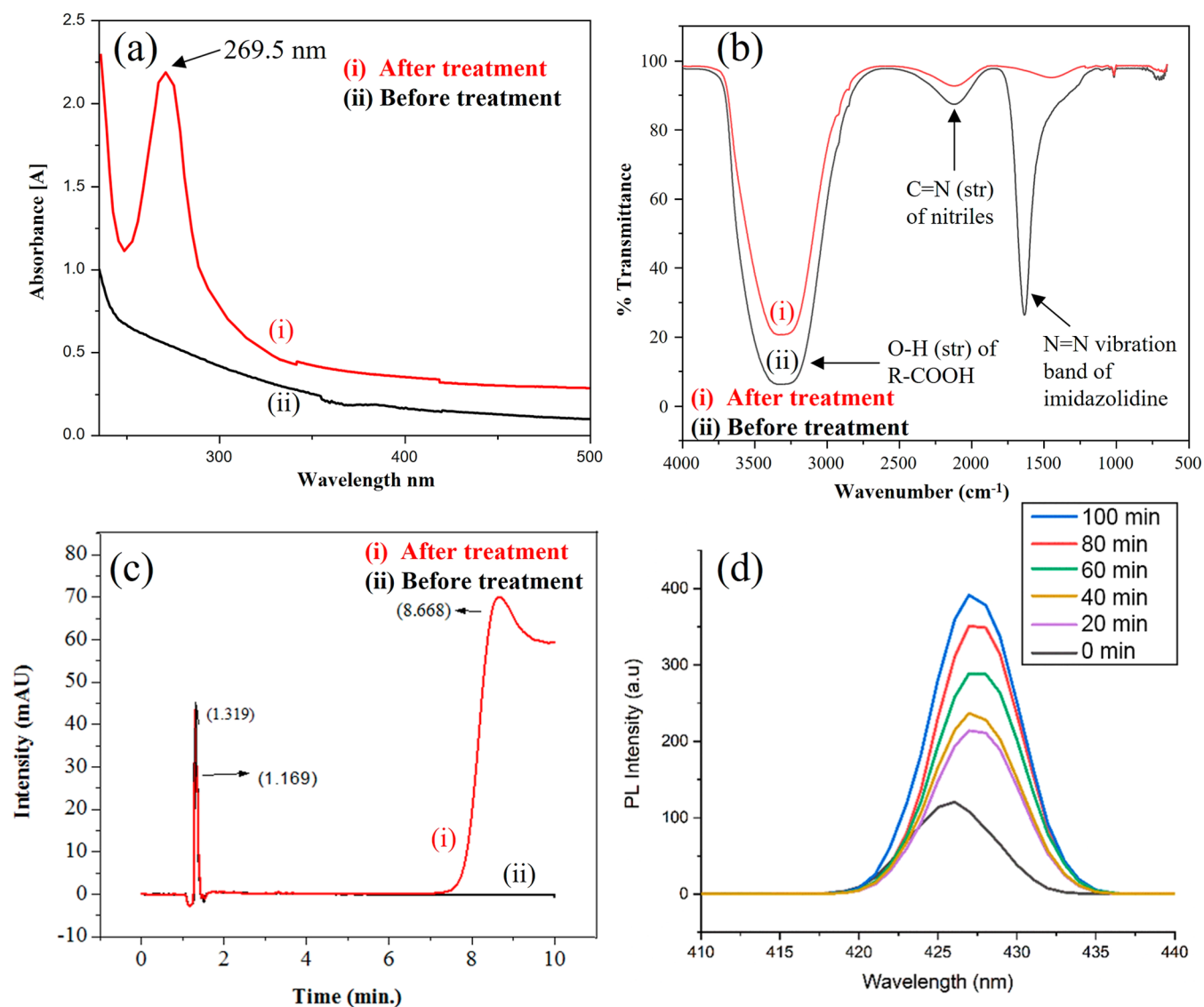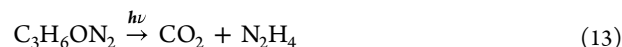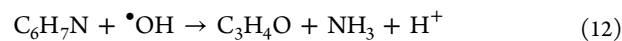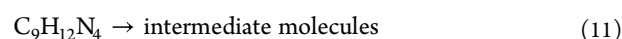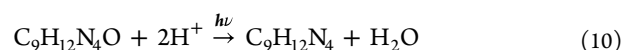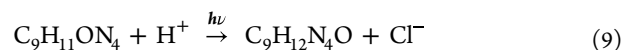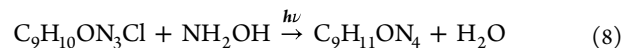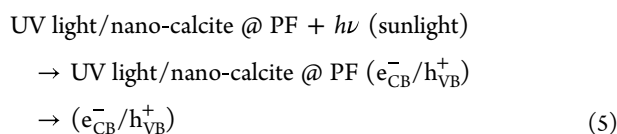**Figure 10.** (a) UV/vis absorbance spectra, (b) FTIR spectra, and (c) HPLC chromatograms of the untreated sample of imidacloprid compared with the treated sample using UV light-irradiated nano-calcite @ PF and (d) time-resolved photoluminescence plot for the emission peak of hydroxy terephthalic acid obtained using UV light-irradiated nano-calcite @ PF.

Table 4. Data Analysis of HPLC Chromatogram for Imidacloprid Solution Treated with UV Light-Irradiated Nano-Calcite @ PF

peak #	retention time (min)	type	width (min)	area (mAU*s)	height (mAU)	area %
before deg	1.721	BB	0.0583	552.72260	86.23747	62.7727
after deg	1.319	BB	0.0659	25.07323	1.43978	7.6473

which further produce $^{\bullet}OH$ and strike with the imidacloprid molecule-bearing water sample.[61] Figure 13 leads to the formation of various reaction intermediates as given by the equations below (5).

$$\text{UV light/nano-calcite @ PF} + h\nu \text{ (sunlight)}$$

$$\rightarrow \text{UV light/nano-calcite @ PF} \ (e^-_{CB}/h^+_{VB})$$

$$\rightarrow (e^-_{CB}/h^+_{VB}) \tag{5}$$

$$e^-_{cb} + O_2 \rightarrow {}^{\bullet}O_2^- \tag{6}$$

$$h^+_{vb} + H_2O \rightarrow {}^{\bullet}OH + H^+ \tag{7}$$

$$C_9H_{10}ON_3Cl + NH_2OH \xrightarrow{h\nu} C_9H_{11}ON_4 + H_2O \tag{8}$$

$$C_9H_{11}ON_4 + H^+ \xrightarrow{h\nu} C_9H_{12}N_4O + Cl^- \tag{9}$$

$$C_9H_{12}N_4O + 2H^+ \xrightarrow{h\nu} C_9H_{12}N_4 + H_2O \tag{10}$$

$$C_9H_{12}N_4 \rightarrow \text{intermediate molecules} \tag{11}$$

$$C_6H_7N + {}^{\bullet}OH \rightarrow C_3H_4O + NH_3 + H^+ \tag{12}$$

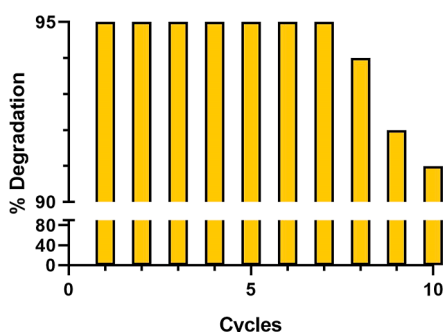$$C_3H_6ON_2 \xrightarrow{h\nu} CO_2 + N_2H_4 \tag{13}$$

Figure 11. Degradation % of imidacloprid for 10 cycles of solar photocatalytic reaction using UV light-irradiated nano-calcite @ PF.

Many studies were conducted to remove pesticides from aqueous solutions as variety of methods removed pollutants under various operational conditions. To compare the results of photolytic and photocatalytic procedures investigated for remediation of pesticides and insecticides, previous reports have been summarized in Table 5.

3. CONCLUSIONS

The presence of imidacloprid in surface water has sparked significant environmental and health concerns. The novel solar photocatalyst, nano-calcite, has been grown on the surface of pretreated and pre-seeded PF by a low-temperature hydrothermal method. The hydrophilic characteristic of the nanocatalyst is increased by irradiation treatments in order to degrade imidacloprid molecules (probe pollutant) by solar photocatalysis. In this context, the photo-induced hydrophilic nature of grafted nano-calcite onto the surface of was achieved by UV and visible light irradiation. After 20 min of UV light irradiation and 3 h of visible light irradiation, nano-calcite @ PF exhibited the highest wickability. Advanced microscopic and spectroscopic techniques such as SEM, TEM, XRD, Zeta potential (ZP), and FTIR were used to determine the morphological characteristics, crystalline structure, surface charge, and functionalities of the as-fabricated and irradiated nanocomposites. The UV- and visible light-irradiation procedures caused photo-induction of hydrophilicity, as revealed by increased roughness of the surface, high crystallinity, high surface −OH concentration, and high photoconductivity (0.724 mS/cm). After the UV−visible light irradiation, nano-calcite @ PF became more hydrophilic and enhanced the photocatalytic degradation of imidacloprid solution. The contact angle reduced from 137.54 to 55.32 and 79° by UV light and visible light irradiation, respectively. The
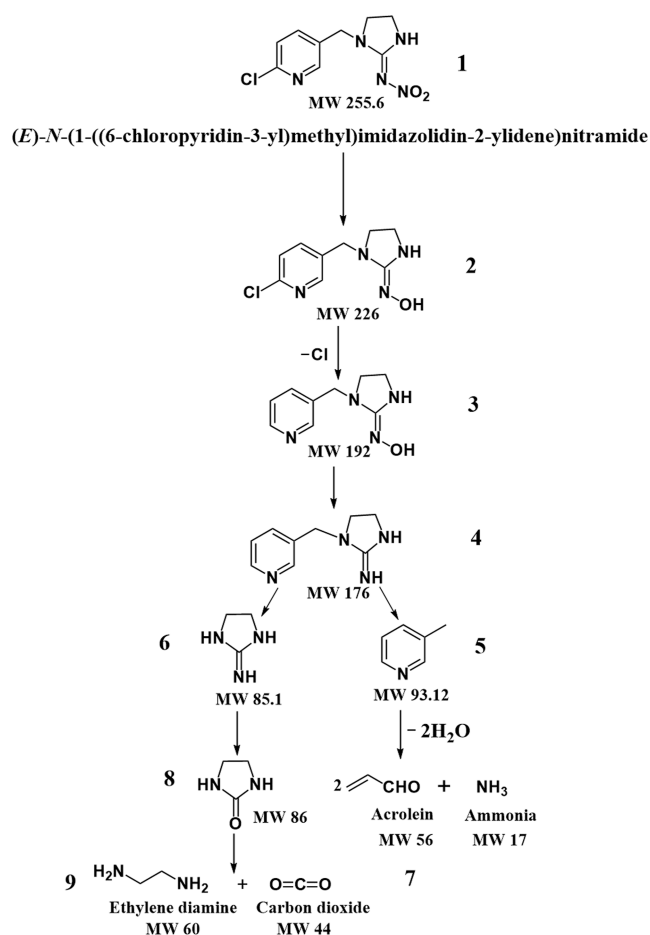

Figure 13. Possible pathways for degradation of imidacloprid using UV light-irradiated nano-calcite @ PF.

roughness of the irradiated nano-calcite @ PF increased due to induction of the −OH group onto the surface of nano-calcite @ PF. The surface charge of nano-calcite became −16.9 and −24.6 mV upon visible light and UV light irradiation, respectively. The decrease in the band gap energy of UV light-treated nano-calcite from 3.5 to 2.95 eV increased the photocatalytic activity in the visible region of solar spectrum. Maximum photocatalytic degradation of imidacloprid observed by UV light-irradiated nano-calcite @ PF and as-fabricated nano-calcite @ PF was 94.15 and 85.50%, respectively. RSM software was utilized to optimize the variable reaction parameters such as oxidant concentration, pH, and sunlight
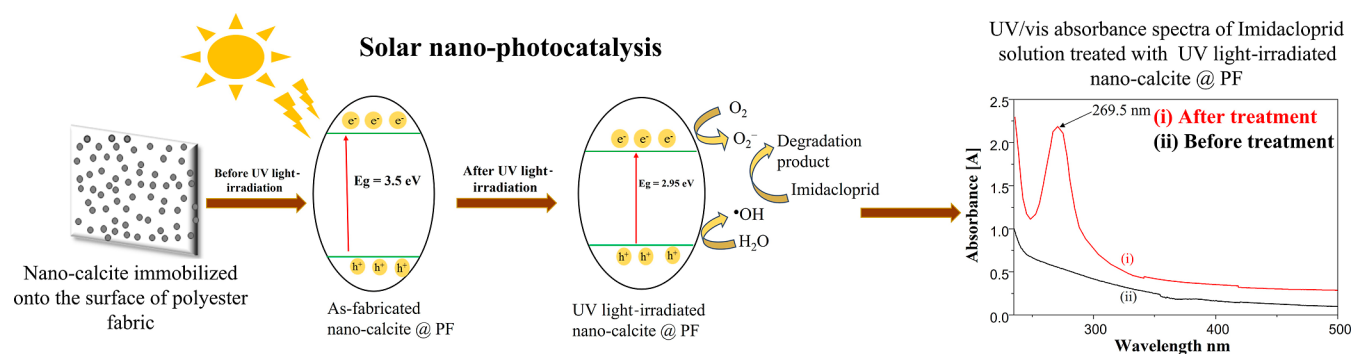

Figure 12. Schematic pathway of solar photocatalytic degradation of imidacloprid by nano-calcite @ PF.

Table 5. Comparison of Previous Studies with Present Investigation for Remediation of Pesticides

photolytic and photocatalytic degradation of pesticides under various operational conditions	catalyst (dose, mg/L)	initial concentration (mg/L)	efficiency (%)	ref
solar photocatalytic degradation of imidacloprid		30	94.15 (degradation)	present study
diazinon photolytic	10	30	57.8 (degradation)	62
diazinon photocatalytic ZnO (100)	10	30	93.3 (degradation)	62
carbofuran photocatalytic TiO_2 (100)	200	300	100 (mineralization)	63
dimethoate photocatalytic TiO_2 (600)	45	160	99 (degradation)	64
lindane photocatalytic $N-TiO_2$ (40)	100	330	100 (degradation)	65
imidacloprid photocatalytic $TiO_2 + Fe^{3+} + H_2O_2$ (500)	20	60	≤76 (degradation)	66
imidacloprid photolytic	255	11	50 (degradation)	67
diazinon photocatalytic ZnO (150)	20	80	80 (degradation)	68
imidacloprid photocatalytic TiO_2 (1000)	10	40	94.4 (degradation)	69
imidacloprid photolytic	100	20	50.45 (degradation)	70
imidacloprid photolytic	10	40	82 (degradation)	69
imidacloprid photocatalytic TiO_2 (100)	100	20	88.15 (degradation)	71
imidacloprid photocatalytic ZnO (100)	100	20	82.17 (degradation)	72

exposure time of the reaction mixture. The photocatalytic degradation rate of imidacloprid solution using mesoporous, UV light-irradiated nano-calcite @ PF was evaluated by UV–visible spectrophotometery, FTIR, and HPLC. The surface of nano-calcite grown onto the PF upon 20 min of irradiation under UV light can render the photocatalyst more hydrophilic with enhanced photocatalytic activity. The time-resolved photoluminescence study has verified the increase in the production of OH radicals with respect to time of exposure to artificial sunlight. The reusability of UV light-treated nano-calcite @ PF has been investigated for 10 cycles of photocatalytic remediation of imidacloprid, indicating the maintenance of high efficiency for 8 cycles. The proposed method seems to be convenient and efficient for the augmentation of the photocatalytic activity of a semiconductor nanomaterial. The remediation of insecticide-bearing wastewater can be performed effectively using this cost-effective and convenient method.

4. METHODS

4.1. Chemicals and Materials.
The chemicals utilized for synthesis were of analytical grade, obtained from commercial sources, and used without further processing. The PF was grafted with nano-calcite on pre-treated and pre-seeded swatches using $Ca(CH_3COO)_2 \cdot 2H_2O$ (99.9%) and KOH (99.9%) at the National Textile University, Faisalabad, Pakistan (Qayyum et al., 2022). Hydrogen peroxide (36% pure H_2O_2) and concentrated HCl and NaOH were obtained from Sigma-Aldrich, and deionized (DI) water was used for preparation of insecticide solution. The insecticide imidacloprid was purchased from the market of Faisalabad Pakistan.

4.2. Surface Grafting of Nano-Calcite onto the Pretreated Polyester Fabric.
Grafting of nano-calcite onto the mercerized and pre-seeded PF was accomplished using the 25 cm² swatches of PF by a low-temperature hydrothermal method.[38] The fabrication of nano-calcite @ PF involved mixing of DI water-based solutions of 225 mL of 0.25 M $Ca(CH_3COO)_2 \cdot 2H_2O$ and 225 mL of 0.35 MKOH while stirring with a magnetic stirrer at 200 rpm. After stirring for 30 min, the reaction mixture was poured into a 500 mL stainless steel jar along with the swatch of pre-seeded PF. The jar was

screwed tightly with a heavy lid and fitted in the socket of Launder-o-meter (TC-M-25) fitted with a revolving steam bath at 90 °C. The reaction contents were subjected to low-temperature hydrothermal conditions for 2.5 hours and then cooled down to room temperature. The swatch of as-fabricated surface-grafted nano-calcite @ PF was rinsed with DI water three times to remove excess of nano-calcite adhered to the surface. Finally, two swatches fabricated were treated with ethanol to remove any impurities, dried at 60 °C in hot air oven for 3 h, and then packed in polythene bags. The powdered nano-calcite obtained from the hydrothermal stainless steel jars was also used for irradiation and characterization.

4.3. Irradiation of Nano-Calcite @ PF with UV and Visible Light.
The swatches of nano-calcite @ PF were cut into (5 × 5 cm²) pieces and irradiated with UV light (low-pressure Hg lamp 72 W at $\lambda = 254$ nm) for a time interval of 5–25 min. The artificial sunlight (D65 = 72 watts) was used as the visible radiation source, and irradiation time was varied from 1 to 5 h. The distance between the containers containing the swatches from the radiation sources was fixed at 75 cm.

4.4. Characterization of Nano-Calcite @ PF.
Multiple techniques were employed to characterize the synthesized material. The crystallinity of as-synthesized nano-calcite @ PF was determined by XRD utilizing Cu Kα irradiation ($\lambda = 1.54$ Å) (Jeol JDX-3532 diffractometer, Japan). The modifications in the morphology were observed by SEM [Quanta 2500. (FEG, USA) and TEM (JEOL 2M 2100, Japan)]. The functional groups present in the functionalized PF were examined by FTIR spectroscopy (Bruker IFS 125HR Japan). Moreover, the surface charge was manifested with the help of zeta potential (Malvern Panalytical, M3-PALS, Malvern, Worcestershire, UK). The variations in the optical characteristics of nano-calcite @ PF were studied by diffused reflectance spectroscopy (Perkin Elmer Lambda 1050, USA), in addition to the band gap energy calculations. The contact angle has been determined to evaluate the hydrophilicity of surface-adhered nano-calcite @ PF using optical tensiometers (Theta Lite/TL100 and TL101, Germany). The determination of the pore distribution and pore size of the nano-calcite sample has been executed by Barret–Joyner–Halenda (BJH) pore size

distribution at 77 K. Prior to the required measurement, degassing was performed for 4 h, under vacuum at 120 °C, in order to evacuate the physiosorbed moisture (Autosorb IQ, Germany).

4.5. Assessment of Comparative Hydrophilicity of Nano-Calcite @ PF.

4.5.1. Wicking Method.

Using the wicking capability of the fabric, the hydrophilicity of as-fabricated and irradiated nano-calcite @ PF was compared. To measure the wickability of the fabric, the DIN 53924 wicking test was used by hanging a swatch of the sample (5×5 cm^2) with a measuring rod.[73] The fabric swatch was hanged vertically in distilled water using a wicking method, and at different time intervals (10 to 60 s), the wicking height of the fabric was measured. As-fabricated as well as UV light and visible light-irradiated nano-calcite @ PF sample swatches were measured by a vertical wicking tester.[74] The water rose up through the strands of functionalized and irradiated PF due to the capillary action against the gravitational force. In order to determine the hydrophilicity of sample, the wicking height was measured with respect to the wicking time in triplets.[38]

4.5.2. Contact Angle Measurement.

To determine the wettability of the surface, the water contact angle of nano-calcite @ PF has been examined by an optical tensiometer (Theta Lite/TL100 and TL101, Germany). The contact angle of as-fabricated as well as UV- and visible light-irradiated swatches of nano-calcite @ PF was determined, and then, the average of the observed values was stated. For contact angle measurement, water was dropped through a syringe (5 μL) and observed as it spread onto the surface-modified nano-calcite @ PF. A video camera was used for the water droplet image dropped using a sessile drop method; the average value of contact angle was reported.[75]

4.6. Photocatalytic Degradation of Imidacloprid.

Photocatalytic degradation of imidacloprid has been performed using glass containers of borosilicate having dimensions ($10 \times 10 \times 4$ cm^3) with a working volume of 100 mL. The photocatalytic degradation of imidacloprid insecticide has been measured during April under the exposure of natural sunlight having an average solar flux of ~600 watts/m^2.[76] The swatches of nano-calcite @ PF were used as a solar photocatalytic reactor under optimized conditions. The (5×5 cm^2) swatches of nano-calcite @ PF were submerged in insecticide solution and exposed to sunlight for 150 min.[77]

4.7. Application of a Statistical Tool for Photocatalytic Reaction.

Response surface methodology via a statistical tool (Design expert 7 pro) has been employed to optimize reaction variables, i.e., reaction time, pH, and concentration of the supporting oxidant (H_2O_2). A 3D response surface was produced by software based on the interactive effect of the independent variable parameters optimized. The rotatable central composite design (RCCD) provided a mathematical relationship to explain the interaction among the three variables (A, B, and C)[78] (Table 6).

Table 6. Coded Reaction Parameters and Ranges of Their Levels Investigated for Optimization

factors	variables	units	low actual	high actual
A	sunlight	hours (h)	1	5
B	pH		9	13
C	oxidant conc. (H_2O_2)	mM	10	50

4.8. Assessment of the Extent of Degradation of Imidacloprid.

The percentage degradation of imidacloprid was evaluated using UV/Visible spectroscopic absorption spectra (CE Cecil 7200, Germany). A UV−visible absorption spectrophotometer (CE Cecil 7200, Germany) was used to monitor the photocatalytic experiments. The absorbance of the irradiated solution was measured by a UV−visible spectrophotometer at 269.5 nm (λ_{max}). Finally, the percentage of imidacloprid photodegradation was calculated using eq 14.

$$\% \text{ degradation} = \left(\frac{X_i - X_f}{X_i} \right) \times 100 \tag{14}$$

where X_i and X_f represent the initial and final absorbance of imidacloprid, respectively.

FTIR spectroscopy was employed to determine the degraded components of imidacloprid. The fragments of the pollutants that appeared after the photocatalytic degradation were also investigated by HPLC (Shimadzu LC-2010C, Markham, Ontario, Canada).

4.9. Determination of OH$^\bullet$ in the Reaction Medium.

For the determination of OH$^\bullet$ radicals produced in the reaction medium as a result of e$^-$/h$^+$ pair generation, the time-resolved photoluminescence experiment was conducted (Spectrofluorometer FS5, Edinburgh Instruments, UK). 100 mL of 0.004 mM terephthalic acid, as a source of fluorescent probe material, was irradiated in a closed reactor with artificial sunlight (72 watts for 100 min). The solution with the UV-irradiated 5×5 cm^2 swatch of the nano-calcite @ PF photocatalyst was experimental, while the solution without the photocatalyst acted as a blank. The fluorescence in the time-resolved experiment was measured using a xenon lamp (150 W at 426 nm) for hydroxy terephthalic acid produced as a product.[59] An aliquot of 3 mL of solution was taken out after every 20 min to measure OH$^\bullet$ generated.[59]

■ AUTHOR INFORMATION

Corresponding Authors

Humera Aziz − Department of Agricultural Sciences, College of Agriculture and Environmental Sciences and Department of Environmental Science, College of Agriculture and Environmental Sciences, Government College University, Faisalabad 38040, Pakistan; Email: humeraaziz.uaf@gmail.com

Zeeshan Ahmad Bhutta − Laboratory of Veterinary Immunology and Biochemistry, College of Veterinary Medicine, Chungbuk National University, Cheongju 28644, Republic of Korea; orcid.org/0000-0002-0148-425X; Email: zee@chungbuk.ac.kr

Authors

Ambreen Ashar − TECS Department, Wilson College of Textiles, NC State University, Raleigh, North Carolina 27606, United States

Ayesha Qayyum − Department of Chemical Engineering (BK21 FOUR Graduate Program), Dong-A University, Busan 49315, Republic of Korea

Ijaz Ahmad Bhatti − Department of Chemistry, University of Agriculture Faisalabad (UAF), Faisalabad 38040, Pakistan

Mostafa A. Abdel-Maksoud − Botany and Microbiology Department, College of Science, King Saud University, Riyadh 11451, Saudi Arabia

Muhammad Hamzah Saleem − *College of Plant Science and Technology, Huazhong Agricultural University, Wuhan 430070, China*

Mohamed R. Eletmany − *TECS Department, Wilson College of Textiles, NC State University, Raleigh, North Carolina 27606, United States; Chemistry Department, Faculty of Science, South Valley University, Qena 83523, Egypt*

Complete contact information is available at:
https://pubs.acs.org/10.1021/acsomega.3c02987

Author Contributions

○A.A. and A.Q. contributed equally to this study and share first authorship.

Notes

The authors declare no competing financial interest.

■ REFERENCES

(1) Jeschke, P.; Nauen, R.; Schindler, M.; Elbert, A. Overview of the status and global strategy for neonicotinoids. *J. Agric. Food Chem.* **2011**, *59*, 2897−2908.

(2) Gervais, J. A.; Luukinen, B.; Buhl, K.; Stone, D. *Imidacloprid Technical Fact Sheet*, 2021;. http://npic.orst.edu/factsheets/archive/imidacloprid.html.

(3) (a) Eng, M. L.; Stutchbury, B. J. M.; Morrissey, C. A. Imidacloprid and chlorpyrifos insecticides impair migratory ability in a seed-eating songbird. *Sci. Rep.* **2017**, *7*, 15176. (b) Millot, F.; Decors, A.; Mastain, O.; Quintaine, T.; Berny, P.; Vey, D.; Lasseur, R.; Bro, E. Field evidence of bird poisonings by imidacloprid-treated seeds: a review of incidents reported by the French SAGIR network from 1995 to 2014. *Environ. Sci. Pollut. Res. Int.* **2017**, *24*, 5469−5485.

(4) Zheng, W.; Liu, W.-p.; Wen, Y.-z.; Lee, S.-J. Photochemistry of insecticide imidacloprid: direct and sensitized photolysis in aqueous medium. *J. Environ. Sci.* **2004**, *16*, 539−542.

(5) (a) Segura, C.; Zaror, C.; Mansilla, H. D.; Mondaca, M. A. Imidacloprid oxidation by photo-Fenton reaction. *J. Hazard. Mater.* **2008**, *150*, 679−686. (b) Yari, K.; Rahmani, A.; Asgari, G.; Azarian, Q.; Bhatnagar, A.; Leili, M. Degradation of imidacloprid pesticide in aqueous solution using an eco-friendly electrochemical process. *Desalin. Water Treat.* **2017**, *86*, 150−157.

(6) (a) Mardare, D.; Cornei, N.; Luca, D.; Dobromir, M.; Irimiciuc, Ş. A.; Pungă, L.; Pui, A.; Adomniţei, C. Synthesis and hydrophilic properties of Mo doped TiO2 thin films. *J. Appl. Phys.* **2014**, *115*, 213501. (b) Kubacka, A.; Fernandez-Garcia, M.; Colon, G. Advanced nanoarchitectures for solar photocatalytic applications. *Chem. Rev.* **2012**, *112*, 1555−1614.

(7) Ashar, A.; Bhutta, Z. A.; Shoaib, M.; Alharbi, N. K.; Fakhar-e-Alam, M.; Atif, M.; Kulyar, M. F.-e-A.; Mahfooz, A.; Boruah, P.; Eletmany, M. R.; Al-Saeed, F. A.; Ezzat Ahmed, A. Cotton fabric loaded with ZnO nanoflowers as a photocatalytic reactor with promising antibacterial activity against pathogenic E. coli. *Arabian Journal of Chemistry* **2023**, *16* (9), 105084.

(8) (a) Hassan, M. M.; Khan, W.; Azam, A.; Naqvi, A. Effect of size reduction on structural and optical properties of ZnO matrix due to successive doping of Fe ions. *J. Lumin.* **2014**, *145*, 160−166. (b) Alveroglu, E.; Balouch, A.; Khan, S.; Mahar, A. M.; Jagirani, M. S.; Pato, A. H. Evaluation of the performance of a selective magnetite molecularly imprinted polymer for extraction of quercetin from onion

samples. *Microchem. J.* **2021**, *162*, 105849. (c) Mahar, A. M.; Balouch, A.; Talpur, F. N.; Panah, P.; Kumar, R.; Kumar, A.; Pato, A. H.; Mal, D.; Kumar, S.; et al. Fabrication of Pt-Pd@ ITO grown heterogeneous nanocatalyst as efficient remediator for toxic methyl parathion in aqueous media. *Environ. Sci. Pollut. Res.* **2020**, *27*, 9970−9978. (d) Fahad; Balouch, A.; Agheem, M. H.; Memon, S. A.; Baloch, A. R.; Tunio, A.; Abdullah; Pato, A. H.; Jagirani, M. S.; Panah, P.; et al. Efficient mitigation of cadmium and lead toxicity in coriander plant utilizing magnetite (Fe3O4) nanofertilizer as growth regulator and antimicrobial agent. *Int. J. Environ. Anal. Chem.* **2020**, *102*, 3868−3879. (e) Pato, A. H.; Balouch, A.; Alveroglu, E.; Buledi, J. A.; Lal, S.; Mal, D. A Practical Non-Enzymatic, Ultra-Sensitive Molybdenum Oxide (MoO3) Electrochemical Nanosensor for Hydroquinone. *J. Electrochem. Soc.* **2021**, *168*, 056503. (f) Mahar, Z. A.; Shar, G. Q.; Balouch, A.; Pato, A. H.; Shaikh, A. R. Effective and viable photocatalytic degradation of Rhodamine B dye in aqueous media using CuO/PVA Nanocomposites. *New J. Chem.* **2021**, *45*, 16500−16510.

(9) (a) Liang, H.; Razaviarani, V.; Buchanan, I. Pesticides and herbicides. *Water Environ. Res.* **2013**, *85*, 1601−1644. (b) Khani, A.; Sohrabi, M. R. Simultaneous synthesis-immobilization of nano ZnO on perlite for photocatalytic degradation of an azo dye in semi batch packed bed photoreactor. *Pol. J. Chem. Technol.* **2012**, *14*, 69−76. (c) Bhadiyadra, J. G.; Vaghani, M. V. A review on applicability of photocatalyst titanium dioxide for treatment of greywater. *Int. J. Eng. Res. Ind. Appl.* **2015**, *5*, 102−105.

(10) Dehghani, M. H.; Fadaei, A. M. Potoccatalytic oxidation of oganophosphorus pesticides using zinc oxide. *Res. J. Chem. Environ.* **2012**, *16*, 104.

(11) Wang, H.; Li, X.; Zhao, X.; Li, C.; Song, X.; Zhang, P.; Huo, P.; Li, X. A review on heterogeneous photocatalysis for environmental remediation: From semiconductors to modification strategies. *Chin. J. Catal.* **2022**, *43*, 178−214.

(12) Sudrajat, H. Superior photocatalytic activity of polyester fabrics coated with zinc oxide from waste hot dipping zinc. *J. Cleaner Prod.* **2018**, *172*, 1722−1729.

(13) Dong, Y.; Bai, Z.; Liu, R.; Zhu, T. Preparation of fibrous TiO2 photocatalyst and its optimization towards the decomposition of indoor ammonia under illumination. *Catal. Today* **2007**, *126*, 320−327.

(14) Afzal, S.; Daoud, W. A.; Langford, S. J. Photostable Self-Cleaning Cotton by a Copper(II) Porphyrin/TiO2 Visible-Light Photocatalytic System. *ACS Appl. Mater. Interfaces* **2013**, *5*, 4753−4759.

(15) Zohoori, S.; Karimi, L.; Ayaziyazdi, S. A novel durable photoactive nylon fabric using electrospun nanofibers containing nanophotocatalysts. *J. Ind. Eng. Chem.* **2014**, *20*, 2934−2938.

(16) Montazer, M.; Behzadnia, A.; Moghadam, M. B. Superior self-cleaning features on wool fabric using TiO2/Ag nanocomposite optimized by response surface methodology. *J. Appl. Polym. Sci.* **2012**, *125*, E356−E363.

(17) Sudrajat, H.; Babel, S.; Sakai, H.; Takizawa, S. Rapid enhanced photocatalytic degradation of dyes using novel N-doped ZrO2. *J. Environ. Manage.* **2016**, *165*, 224−234.

(18) Sudrajat, H.; Babel, S. A new, cost-effective solar photoactive system N-ZnO@polyester fabric for degradation of recalcitrant compound in a continuous flow reactor. *Mater. Res. Bull.* **2016**, *83*, 369−378.

(19) Kim, S.; Kafi, A. A.; Bafekpour, E.; Lee, Y.-I.; Fox, B.; Hussain, M.; Choa, Y.-H. Wettability investigation of UV/O3 and acid functionalized MWCNT and MWCNT/PMMA nanocomposites by contact angle measurement. *J. Nanomater.* **2015**, *2015*, 1−12.

(20) Nakamura, M.; Sirghi, L.; Aoki, T.; Hatanaka, Y. Study on hydrophilic property of hydro-oxygenated amorphous TiO x: OH thin films. *Surf. Sci.* **2002**, *507*−*510*, 778−782.

(21) Park, H.; Choi, W. Effects of TiO2 surface fluorination on photocatalytic reactions and photoelectrochemical behaviors. *J. Phys. Chem. B* **2004**, *108*, 4086−4093.

(22) Emeline, A. V.; Rudakova, A. V.; Sakai, M.; Murakami, T.; Fujishima, A. Factors affecting UV-induced superhydrophilic conversion of a TiO2 surface. *J. Phys. Chem. C* **2013**, *117*, 12086−12092.

(23) Pandiyaraj, K. N.; Selvarajan, V. Non-thermal plasma treatment for hydrophilicity improvement of grey cotton fabrics. *J. Mater. Process. Technol.* **2008**, *199*, 130−139.

(24) (a) Miyauchi, M.; Kieda, N.; Hishita, S.; Mitsuhashi, T.; Nakajima, A.; Watanabe, T.; Hashimoto, K. Reversible wettability control of TiO2 surface by light irradiation. *Surf. Sci.* **2002**, *511*, 401−407. (b) Madaeni, S.; Ghaemi, N. Characterization of self-cleaning RO membranes coated with TiO2 particles under UV irradiation. *J. Membr. Sci.* **2007**, *303*, 221−233. (c) Janczarek, M.; Hupka, J.; Kisch, H. Hydrophilicity of TiO2 exposed to UV and VIS radiation. *Physicochem. Probl. Miner. Process.* **2006**, *40*, 287−292. (d) Uosaki, K.; Yano, T.; Nihonyanagi, S. Interfacial water structure at as-prepared and UV-induced hydrophilic TiO2 surfaces studied by sum frequency generation spectroscopy and quartz crystal microbalance. *J. Phys. Chem. B* **2004**, *108*, 19086−19088. (e) Zhang, L.; Dillert, R.; Bahnemann, D.; Vormoor, M. Photo-induced hydrophilicity and self-cleaning: models and reality. *Energy & Environmental Science* **2012**, *5*, 7491−7507. (f) Rudakova, A. V.; Maevskaya, M. V.; Emeline, A. V.; Bahnemann, D. W. Light-Controlled ZrO2 Surface Hydrophilicity. *Sci. Rep.* **2016**, *6*, 34285.

(25) Sakai, N.; Fujishima, A.; Watanabe, T.; Hashimoto, K. Enhancement of the photoinduced hydrophilic conversion rate of TiO2 film electrode surfaces by anodic polarization. *J. Phys. Chem. B* **2001**, *105*, 3023−3026.

(26) Kim, S.; Kafi, A. A.; Bafekpour, E.; Lee, Y.-I.; Fox, B.; Hussain, M.; Choa, Y.-H. Wettability investigation of UV/O3 and acid functionalized MWCNT and MWCNT/PMMA nanocomposites by contact angle measurement. *J. Nanomater.* **2015**, *16*, 3.

(27) Ghanashyam Krishna, M.; Vinjanampati, M.; Dhar Purkayastha, D. Metal oxide thin films and nanostructures for self-cleaning applications: current status and future prospects. *Eur. Phys. J.: Appl. Phys.* **2013**, *62*, 30001.

(28) Talinungsang, N. P.; Purkayastha, D. D. SnO2/TiO2 bilayer thin films exhibiting superhydrophilic properties. In *AIP Conference Proceedings*; AIP Publishing, 2017; Vol. *1832*, p 080035.

(29) Li, H.; Gong, Y.; Huang, Q.; Zhang, H. Degradation of Orange II by UV-assisted advanced Fenton process: response surface approach, degradation pathway, and biodegradability. *Ind. Eng. Chem. Res.* **2013**, *52*, 15560−15567.

(30) (a) Li, H.; Shang, J.; Yang, Z.; Shen, W.; Ai, Z.; Zhang, L. Oxygen vacancy associated surface Fenton chemistry: surface structure dependent hydroxyl radicals generation and substrate dependent reactivity. *Environ. Sci. Technol.* **2017**, *51*, 5685−5694. (b) Tae Kwon, Y.; Yong Song, K.; In Lee, W.; Jin Choi, G.; Rag Do, Y. Photocatalytic behavior of WO3-loaded TiO2 in an oxidation reaction. *J. Catal.* **2000**, *191*, 192−199.

(31) de Leeuw, N. H.; Parker, S. C. Surface structure and morphology of calcium carbonate polymorphs calcite, aragonite, and vaterite: an atomistic approach. *J. Phys. Chem. B* **1998**, *102*, 2914−2922.

(32) Atasağun, H.G.; Okur, A.; Akkan, T.; Akkan, L.Ö. A test apparatus to measure vertical wicking of fabrics − a case study on shirting fabrics. *Journal of the Textile Institute* **2016**, *107* (12), 1483−1489.

(33) Dong, Y.; Kong, J.; Phua, S. L.; Zhao, C.; Thomas, N. L.; Lu, X. Tailoring Surface Hydrophilicity of Porous Electrospun Nanofibers to Enhance Capillary and Push−Pull Effects for Moisture Wicking. *ACS Appl. Mater. & Inter.* **2014**, *6* (16), 14087−14095.

(34) Widyastuti, S. Synthesis and characterization of CaCO3 (calcite) nano particles from cockle shells (Anadara granosa Linn) by precipitation method. In *AIP Conference Proceedings*; AIP Publishing LLC, 2017; Vol. *1855*, p 030018.

(35) Barhoum, A.; Van Assche, G.; Makhlouf, A. S. H.; Terryn, H.; Baert, K.; Delplancke, M.-P.; El-Sheikh, S. M.; Rahier, H. A green, simple chemical route for the synthesis of pure nanocalcite crystals. *Cryst. Growth Des.* **2015**, *15*, 573−580.

(36) Kamel, M.; El Zawahry, M.; Helmy, H.; Eid, M. Improvements in the dyeability of polyester fabrics by atmospheric pressure oxygen plasma treatment. *J. Text. Inst.* **2011**, *102*, 220−231.

(37) Nadeem, F.; Bhatti, I. A.; Ashar, A.; Yousaf, M.; Iqbal, M.; Mohsin, M.; Nisar, J.; Tamam, N.; Alwadai, N. Eco-benign biodiesel production from waste cooking oil using eggshell derived MM-CaO catalyst and condition optimization using RSM approach. *Arabian J. Chem.* **2021**, *14*, 103263.

(38) Qayyum, A.; Bhatti, I. A.; Ashar, A.; Jilani, A.; Iqbal, J.; Mohsin, M.; Ishaq, T.; Muhammad, S.; Wageh, S.; Dustgeer, M. R. Prewetting Induced Hydrophilicity to Augment Photocatalytic Activity of Nanocalcite @ Polyester Fabric. *Polymers* **2022**, *14*, 295.

(39) Al Mahrouqi, D.; Vinogradov, J.; Jackson, M. D. Zeta potential of artificial and natural calcite in aqueous solution. *Adv. Colloid Interface Sci.* **2017**, *240*, 60−76.

(40) Buszewski, B.; Pomastowski, P. Wpływ heterogeniczności powierzchni biokoloidów na ich rozdzielanie elektroforetyczne. *Wiadomości chemiczne* **2015**, *69*, 823−846.

(41) Li, S.; Leroy, P.; Heberling, F.; Devau, N.; Jougnot, D.; Chiaberge, C. Influence of surface conductivity on the apparent zeta potential of calcite. *J. Colloid Interface Sci.* **2016**, *468*, 262−275.

(42) Bai, J.; Shen, R.; Jiang, Z.; Zhang, P.; Li, Y.; Li, X. Integration of 2D layered CdS/WO3 S-scheme heterojunctions and metallic Ti3C2 MXene-based Ohmic junctions for effective photocatalytic H2 generation. *Chin. J. Catal.* **2022**, *43*, 359−369.

(43) Zhou, D.; Wang, L.; Zhang, F.; Wu, J.; Wang, H.; Yang, J. Feasible Degradation of Polyethylene Terephthalate Fiber-Based Microplastics in Alkaline Media with Bi2O3@N-TiO2 Z-Scheme Photocatalytic System. *Adv. Sustainable Syst.* **2022**, *6*, 2100516.

(44) Norek, M. Approaches to enhance UV light emission in ZnO nanomaterials. *Curr. Appl. Phys.* **2019**, *19*, 867−883.

(45) Li, L.-X.; Chen, C.; Li, Z.-H.; Wang, F.-F.; Liu, Y.; Yi, Z.-G. Controllable Synthesis, Polar Behavior and Photoelectric Properties of BiOCl Microplates. *Chin. J. Struct. Chem.* **2022**, *41*, 2203077−2203084.

(46) Mohsin, M.; Bhatti, I. A.; Ashar, A.; Mahmood, A.; Hassan, Q. u.; Iqbal, M. Fe/ZnO@ ceramic fabrication for the enhanced photocatalytic performance under solar light irradiation for dye degradation. *J. Mater. Res. Technol.* **2020**, *9*, 4218−4229.

(47) Ashar, A.; Bhatti, I. A.; Ashraf, M.; Tahir, A. A.; Aziz, H.; Yousuf, M.; Ahmad, M.; Mohsin, M.; Bhutta, Z. A. Fe3+@ ZnO/ polyester based solar photocatalytic membrane reactor for abatement of RB5 dye. *J. Cleaner Prod.* **2020**, *246*, 119010.

(48) (a) Fokoua, E. N.; Poletti, F.; Richardson, D. J. Analysis of light scattering from surface roughness in hollow-core photonic bandgap fibers. *Opt. Express* **2012**, *20*, 20980−20991. (b) Bauer, J. Optical properties, band gap, and surface roughness of Si3N4. *Phys. Status Solidi A* **1977**, *39*, 411−418. (c) Liu, Z.; Tian, J.; Yu, C.; Fan, Q.; Liu, X. Solvothermal fabrication of Bi2MoO6 nanocrystals with tunable oxygen vacancies and excellent photocatalytic oxidation performance in quinoline production and antibiotics degradation. *Chin. J. Catal.* **2022**, *43*, 472−484.

(49) Ashar, A.; Iqbal, M.; Bhatti, I. A.; Ahmad, M. Z.; Qureshi, K.; Nisar, J.; Bukhari, I. H. Synthesis, characterization and photocatalytic activity of ZnO flower and pseudo-sphere: Nonylphenol ethoxylate degradation under UV and solar irradiation. *J. Alloys Compd.* **2016**, *678*, 126−136.

(50) (a) Nakamura, M.; Sirghi, L.; Aoki, T.; Hatanaka, Y. Study on hydrophilic property of hydro-oxygenated amorphous TiOx: OH thin films. *Surf. Sci.* **2002**, *507−510*, 778−782. (b) Wang, R.; Sakai, N.; Fujishima, A.; Watanabe, T.; Hashimoto, K. Studies of surface wettability conversion on TiO2 single-crystal surfaces. *J. Phys. Chem. B* **1999**, *103*, 2188−2194.

(51) (a) Chen, Y.; Analytis, J. G.; Chu, J.-H.; Liu, Z.; Mo, S.-K.; Qi, X.-L.; Zhang, H.; Lu, D.; Dai, X.; Fang, Z.; et al. Experimental realization of a three-dimensional topological insulator, Bi2Te3. *science* **2009**, *325*, 178−181. (b) Chen, Y.; Chen, F.; Zhang, J. Effect

of surface fluorination on the photocatalytic and photo-induced hydrophilic properties of porous TiO2 films. *Appl. Surf. Sci.* **2009**, *255*, 6290−6296.

(52) Wang, W.; Zhang, H.; Chen, Y.; Shi, H. Efficient degradation of tetracycline via coupling of photocatalysis and photo-Fenton processes over a 2D/2D α-Fe2O3/g-C3N4 S-scheme heterojunction catalyst. *Acta Phys.-Chim. Sin.* **2022**, *38*, 2201008.

(53) Zhao, Y.; Qin, X.; Zhao, X.; Wang, X.; Tan, H.; Sun, H.; Yan, G.; Li, H.; Ho, W.; Lee, S.-c. Polyoxometalates-doped Bi2O3−/Bi photocatalyst for highly efficient visible-light photodegradation of tetrabromobisphenol A and removal of NO. *Chin. J. Catal.* **2022**, *43*, 771−781.

(54) Zhou, L.; Li, Y.; Zhang, Y.; Qiu, L.; Xing, Y. A 0D/2D Bi4V2O11/g-C3N4 S-scheme heterojunction with rapid interfacial charges migration for photocatalytic antibiotic degradation. *Acta Phys.-Chim. Sin.* **2022**, *38*, 2112027.

(55) (a) Quintás, G.; Armenta, S.; Garrigues, S.; Guardia, M. d. l. Fourier transform infrared determination of imidacloprid in pesticide formulations. *J. Braz. Chem. Soc.* **2004**, *15*, 307−312. (b) Phugare, S. S.; Kalyani, D. C.; Gaikwad, Y. B.; Jadhav, J. P. Microbial degradation of imidacloprid and toxicological analysis of its biodegradation metabolites in silkworm (Bombyx mori). *Chem. Eng. J.* **2013**, *230*, 27−35.

(56) Al-Rimawi, F. A HPLC-UV method for determination of three pesticides in water. *Int. J. Adv. Pharm., Biol. Chem.* **2014**, *2*, 1−8.

(57) (a) Ishii, Y.; Kobori, I.; Araki, Y.; Kurogochi, S.; Iwaya, K.; Kagabu, S. HPLC determination of the new insecticide imidacloprid and its behavior in rice and cucumber. *J. Agric. Food Chem.* **1994**, *42*, 2917−2921. (b) Iqbal, S.; Uddin, R.; Saied, S.; Ahmed, M.; Abbas, M.; Aman, S. Extraction, cleanup, and chromatographic determination of imidacloprid residues in wheat. *Bull. Environ. Contam. Toxicol.* **2012**, *88*, 555−558.

(58) Wamhoff, H.; Schneider, V. Photodegradation of imidacloprid. *J. Agric. Food Chem.* **1999**, *47*, 1730−1734.

(59) Lavand, A. B.; Malghe, Y. S. Synthesis, characterization and visible light photocatalytic activity of carbon and iron modified ZnO. *J. King Saud Univ., Sci.* **2018**, *30*, 65−74.

(60) Li, N.; Ma, J.; Zhang, Y.; Zhang, L.; Jiao, T. Recent Developments in Functional Nanocomposite Photocatalysts for Wastewater Treatment: A Review. *Adv. Sustainable Syst.* **2022**, *6*, 2200106.

(61) Garg, R.; Gupta, R.; Bansal, A. Photocatalytic degradation of imidacloprid using semiconductor hybrid nano-catalyst: kinetics, surface reactions and degradation pathways. *Int. J. Environ. Sci. Technol.* **2021**, *18*, 1425−1442.

(62) Moussavi, G.; Hossaini, H.; Jafari, S. J.; Farokhi, M. Comparing the efficacy of UVC, UVC/ZnO and VUV processes for oxidation of organophosphate pesticides in water. *J. Photochem. Photobiol., A* **2014**, *290*, 86−93.

(63) Mahalakshmi, M.; Arabindoo, B.; Palanichamy, M.; Murugesan, V. Photocatalytic degradation of carbofuran using semiconductor oxides. *J. Hazard. Mater.* **2007**, *143*, 240−245.

(64) Chen, J.-Q.; Wang, D.; Zhu, M.-X.; Gao, C.-J. Photocatalytic degradation of dimethoate using nanosized TiO2 powder. *Desalination* **2007**, *207*, 87−94.

(65) Senthilnathan, J.; Philip, L. Photocatalytic degradation of lindane under UV and visible light using N-doped TiO2. *Chem. Eng. J.* **2010**, *161*, 83−92.

(66) Kitsiou, V.; Filippidis, N.; Mantzavinos, D.; Poulios, I. Heterogeneous and homogeneous photocatalytic degradation of the insecticide imidacloprid in aqueous solutions. *Appl. Catal., B* **2009**, *86*, 27−35.

(67) Ding, T.; Jacobs, D.; Lavine, B. K. Liquid chromatography-mass spectrometry identification of imidacloprid photolysis products. *Microchem. J.* **2011**, *99*, 535−541.

(68) Daneshvar, N.; Aber, S.; Seyed Dorraji, M. S.; Khataee, A. R.; Rasoulifard, M. H. Photocatalytic degradation of the insecticide diazinon in the presence of prepared nanocrystalline ZnO powders under irradiation of UV-C light. *Sep. Purif. Technol.* **2007**, *58*, 91−98.

(69) Nikoonahad, A.; Djahed, B.; Norzaee, S.; Eslami, H.; Derakhshan, Z.; Miri, M.; Fakhri, Y.; Hoseinzadeh, E.; Ghasemi, S. M.; Balarak, D.; et al. An overview report on the application of heteropoly acids on supporting materials in the photocatalytic degradation of organic pollutants from aqueous solutions. *PeerJ* **2018**, *6*, No. e5501.

(70) Pandey, S.; Giri, K.; Kumar, R.; Mishra, G.; Raja Rishi, R. Nanopesticides: opportunities in crop protection and associated environmental risks. *Proc. Natl. Acad. Sci., India, Sect. B* **2018**, *88*, 1287−1308.

(71) Saravanan, A.; Kumar, P. S.; Jeevanantham, S.; Anubha, M.; Jayashree, S. Degradation of toxic agrochemicals and pharmaceutical pollutants: Effective and alternative approaches toward photocatalysis. *Environ. Pollut.* **2022**, *298*, 118844.

(72) Yeganeh, M.; Charkhloo, E.; Sobhi, H. R.; Esrafili, A.; Gholami, M. Photocatalytic processes associated with degradation of pesticides in aqueous solutions: Systematic review and meta-analysis. *Chem. Eng. J.* **2022**, *428*, 130081.

(73) Atasağun, H. G.; Okur, A.; Akkan, T.; Akkan, L. Ö. A test apparatus to measure vertical wicking of fabrics − a case study on shirting fabrics. *J. Text. Inst.* **2016**, *107*, 1483−1489.

(74) (a) Ferrero, F. Wettability measurements on plasma treated synthetic fabrics by capillary rise method. *Polym. Test.* **2003**, *22*, 571−578. (b) Nithya, E.; Radhai, R.; Rajendran, R.; Shalini, S.; Rajendran, V.; Jayakumar, S. Synergetic effect of DC air plasma and cellulase enzyme treatment on the hydrophilicity of cotton fabric. *Carbohydr. Polym.* **2011**, *83*, 1652−1658.

(75) Abdi, Y.; Khalilian, M.; Arzi, E. Enhancement in photo-induced hydrophilicity of TiO2/CNT nanostructures by applying voltage. *J. Phys. D: Appl. Phys.* **2011**, *44*, 255405.

(76) (a) Zaidi, B. Introductory chapter: Introduction to photovoltaic effect. In *Solar Panels and Photovoltaic Materials*; InTech Open: London, UK, 2018; pp 1−8. (b) Belessiotis, V.; Kalogirou, S.; Delyannis, E.; Belessiotis, V.; Kalogirou, S.; Delyannis, E. Chapter Six−Indirect Solar Desalination (MSF, MED, MVC, TVC). *Thermal Solar Desalination*; Academic Press, 2016; pp 283-326.

(77) (a) Chang, C.; Tao, P.; Xu, J.; Fu, B.; Song, C.; Wu, J.; Shang, W.; Deng, T. High-Efficiency Superheated Steam Generation for Portable Sterilization under Ambient Pressure and Low Solar Flux. *ACS Appl. Mater. Interfaces* **2019**, *11*, 18466−18474. (b) Liu, X.; Wu, X.; Long, Z.; Zhang, C.; Ma, Y.; Hao, X.; Zhang, H.; Pan, C. Photodegradation of imidacloprid in aqueous solution by the metal-free catalyst graphitic carbon nitride using an energy-saving lamp. *J. Agric. Food Chem.* **2015**, *63*, 4754−4760.

(78) Im, J.-K.; Cho, I.-H.; Kim, S.-K.; Zoh, K.-D. Optimization of carbamazepine removal in O3/UV/H2O2 system using a response surface methodology with central composite design. *Desalination* **2012**, *285*, 306−314.